

Inverse and direct cascade of kinetic and potential energy for self-gravitating collisionless dark matter flow and effects of halo shape on energy cascade

Zhijie (Jay) Xu<sup>1,a</sup>

1. Computational Mathematics Group, Physical and Computational Sciences Directorate, Pacific Northwest National Laboratory, Richland, WA 99352, USA

Abstract:

Halo-mediated inverse mass cascade and associated energy cascade are key features to understand self-gravitating collisionless dark matter flow (SG-CFD). This paper formulates the energy cascade that is deeply connected with the mass cascade. Both cascade origin from the continuous mass exchange between halo and out-of-halo sub-systems. Kinetic energy can be divided into contributions from motion of halo and the motion in halo, while potential energy can be decomposed into inter- and intra-halo interactions accordingly. The intra-halo virial equilibrium is established much faster for particle motion in halos than the inter-halo equilibrium for motion of halos. Total energy in out-of-halo sub-system is conserved with time such that all energy change of entire system comes from the virialization in halos. At statistically steady state, a continuous mass exchange between two sub-systems at the smallest mass scale is required to sustain the growth of total halo mass as  $M_h \sim a^{1/2}$  and halo energy  $E \sim a^{3/2}$ , i.e. a decreasing mass flux  $\epsilon_m \sim a^{-1}$  and a constant energy flux, where  $a$  is scale factor. By introducing the energy flux and transfer functions, an inverse cascade of kinetic energy is identified where kinetic energy is injected at the smallest scale and continuously transferred to large scales. This is sustained by the direct cascade of potential energy from large to small mass scale. Two cascades are related by the virial theorem. Both kinetic and potential energies exhibit a scale- and time-independent flux in mass propagation

---

<sup>a)</sup> Electronic mail: [zhijie.xu@pnnl.gov](mailto:zhijie.xu@pnnl.gov); [zhijiexu@hotmail.com](mailto:zhijiexu@hotmail.com)

range with energy flux proportional to the mass flux. The energy cascade is mostly facilitated by mass cascade and mass accretion. It can also be quantitatively described using the concept of typical halos that grow with a constant waiting time. By correctly modeling the dependence of halo radial and rotational moment and angular velocity on halo mass, an inverse cascade can also be identified for the kinetic energy from coherent radial and rotational motion (mean flow) in halos. For a given mass of halos, the rotational kinetic energy is independent of time, while the radial (peculiar) kinetic energy decreases with time.

In hydrodynamic turbulence, the vortex stretching (shape changing) along its axis of rotation facilitates the energy cascade from large to small length scale. Vortex is generally volume-conserved with uniform density due to incompressibility. The axis of vortex rotation is usually aligned with the major axis of that vortex. By contrast, halos are dynamically growing, rotating, and shape changing objects with a nonuniform density. The effect of halo shape change does not play a significant role in energy cascade with halo moment of inertial gained from shape change being less than 2 times. Large halos exhibit a range of shapes with a preference for prolateness over oblateness and most halos have their spin axis lying perpendicular to major axis. Since mass cascade is local in mass space, the shape of halos should also evolve continuously in mass space with large halo formed by incrementally inheriting its shape/structure from progenitor halo. A unique evolution path for halo structure can be identified that gradually approaches spherical shape with increasing halo size.

Key Words: Dark Matter Halo, Dark Matter Flow, Collisionless, Energy Cascade, Self-gravitating, Halo Shape

## Contents

|  |    |
|--|----|
| Nomenclature .....   | 4  |
| 1. Introduction .....  | 5  |
| 2. The simulation and numerical data .....                               | 9  |
| 3. Real-space inverse mass cascade of SG-CFD .....                       | 9  |
| 4. Real-space energy cascade of SG-CFD .....                             | 15 |
| 4.1 Inverse cascade of halo kinetic energy .....                         | 15 |
| 4.2 A general formulation for cascade of a specific quantity .....       | 21 |
| 4.3 Inverse cascade of virial kinetic energy .....                       | 24 |
| 4.4 Direct cascade of halo potential energy .....                        | 26 |
| 4.5 The temporal evolution of total kinetic and potential energies ..... | 31 |
| 4.6 Inverse cascade of halo radial and rotational kinetic energy .....   | 36 |
| 5. The effect of halo shape on energy cascade.....                       | 44 |
| 6. Conclusion.....   | 53 |

## **Nomenclature**

See Supplementary Information

## 1. Introduction

The self-gravitating collisionless fluid dynamics (SG-CFD) concerns the motion of collisionless matter due to its own gravity. In physics, “collisionless” refers to a matter with extremely low interaction cross-section such that the collisions between particles have no effects on the system dynamics. Typical examples can be the cold dark matter and low-density plasmas under high magnetic field. The gravitational collapse of collisionless particles is a good example of the nonlinear SG-CFD problem, where gravitational instability leads to the structure formation and evolution. The inverse mass cascade is a key feature of self-gravitating collisionless flow (SG-CFD) that is not present in regular hydrodynamic turbulence [1, 2]. However, both problems involve energy cascade through different scales.

Turbulence is ubiquitous in nature and represents one of the most challenging and fascinating problems in classical physics, where the difficulty mostly stems from the random and nonlinear nature with inherent presence of many inseparable scales. To understand the energy cascade in SG-CFD, it should be beneficial by revisiting some fundamental ideas in turbulence. The classical picture of turbulence is a cascade process, where large eddies feed smaller eddies, which feed even smaller eddies, and so on to the smallest scale where viscous dissipation is dominant, i.e. the concept of a direct (kinetic) energy cascade [3]. For incompressible turbulence, the energy cascade starts with the kinetic energy obtained from mean flow by the largest eddies through Reynolds stress (arising from velocity fluctuations). The kinetic energy continuously transferred from mean flow to random motion of turbulence and further transferred successively down to smaller and smaller eddies until the viscous dissipation becomes dominant (collisions between molecules).

In 1940s, Kolmogorov opened the way for a rigorous quantitative description of energy cascade based on similarity principles [4, 5]. For three-dimensional incompressible flow with high

Reynolds number (or negligible viscosity), the energy transfer from mean flow and cascade across scales proceed through a “vortex stretching” mechanism [6, 7]. In the presence of shear stress in mean flow, the Reynolds stress due to velocity fluctuation [8] acts as a conduit to continuously draw energy from mean flow and sustain the energy cascade in turbulence. The equation for vorticity  $\boldsymbol{\omega}$  of a three-dimensional incompressible flow reads,

$$\frac{\partial \boldsymbol{\omega}}{\partial t} + (\mathbf{u} \cdot \nabla) \boldsymbol{\omega} = \underbrace{(\boldsymbol{\omega} \cdot \nabla) \mathbf{u}}_1 + \nu \nabla^2 \boldsymbol{\omega}, \quad (1)$$

where term 1 leads to the vortex stretching. Here  $\mathbf{u}$  is the velocity field and vortices’ volume is assumed to be conserved for incompressible flow. The shear stress induced lengthening of vortices along the direction of vorticity vector ( $\boldsymbol{\omega} = \nabla \times \mathbf{u}$ ) implies a thinning of the fluid element in the direction perpendicular to the stretching. This will intensify the vorticity with rising kinetic energy due to the conservation of angular momentum when viscous effect is negligible.

Let’s assume a volume conserved fluid element with moment of inertial  $I_1, I_2$  and vorticity  $\omega_1, \omega_2$  right before and after vortex stretching. The ratio of kinetic energy from the conservation of angular momentum  $I_1 \omega_1 = I_2 \omega_2$  is

$$\frac{I_2 \omega_2^2}{I_1 \omega_1^2} = \frac{I_1}{I_2}, \quad (2)$$

where a smaller moment of inertial about the axis of rotating after stretching ( $I_2 < I_1$ ) leads to a greater vorticity ( $\omega_2 > \omega_1$ ) and a rising rotational kinetic energy. With vortices teased out into thinner and thinner filaments, kinetic energy is passed down to smaller and smaller scales and finally dissipated by the molecular viscosity. For high-Re number flow with a vanishing viscosity  $\nu \rightarrow 0$ , enstrophy ( $|\boldsymbol{\omega}|^2$ , the square of vorticity) can be unbounded and approach infinity. However,

the rate of energy dissipation (proportional to  $\nu|\boldsymbol{\omega}|^2$ ) is still finite even with  $\nu \rightarrow 0$  such that the total kinetic energy decreases with time.

While direct energy cascade is a dominant feature for 3D turbulence, the two-dimensional turbulence exhibits an inverse energy cascade. In fact, there exists a range of length scales over which kinetic energy is transferred from small to large scales for two-dimensional turbulence, i.e. an inverse energy cascade predicted in the late 1960s [9]. The two-dimensional turbulence is not just simply a reduced-dimension version of three-dimensional turbulence. New conservation laws in two-dimension flow leads to a completely different phenomenology. Note that the vorticity vector  $\boldsymbol{\omega}$  reduces to a scalar  $\omega$  in 2D (or always perpendicular to velocity field  $\mathbf{u}$ ), vortex stretching cannot work (term 1 in Eq. (1) is not present for 2D). The total system enstrophy ( $\omega^2$ ) in a two-dimensional flow is destroyed by viscosity and should monotonically decrease with time. The enstrophy is bounded from above by its initial value. For a high-Re two-dimensional incompressible flow with viscosity  $\nu \rightarrow 0$ , the energy dissipation rate  $\nu\omega^2 \rightarrow 0$  which is finite in 3D incompressible flow. The enstrophy  $\omega^2$  in 2D flow is a bounded quantity such that the total system energy is nearly conserved with energy dissipation rate  $\nu\omega^2 \rightarrow 0$ . However, the rate of enstrophy dissipation (proportional to  $\nu(\nabla\omega)^2$ ) can be finite with palinstrophy ( $(\nabla\omega)^2$ ) unbounded and approaching infinity. The kinetic energy ( $|\mathbf{u}|^2$ ) is nearly conserved, while the enstrophy  $\omega^2$  is dissipated in high-Re two-dimensional turbulence. The vorticity  $\omega$  simply replaces the role of  $\mathbf{u}$  in three-dimensional turbulence.

It turns out that a fully developed two-dimensional turbulence has: a direct cascade of enstrophy ( $\omega^2$ ) from large to small scales and an inverse cascade of kinetic energy ( $u^2$ ) from small to large scales. As flow develops, the enstrophy is continually passed down to the small scales,

where it is destroyed by viscosity. While it is not possible for vortex stretching to operate in two-dimensional flow, vorticity is a materially conserved quantity and simply advected like a passive scalar to create a continuous filamentation of the vorticity for high-Re incompressible flow. Continuously area-conserved teasing and twisting make vortex patches thinner and longer that facilitates a combined direct cascade of enstrophy and inverse cascade of kinetic energy.

Based on this brief description for energy/enstrophy cascade, let us turn to some unique features of SG-CFD, and their fundamental effects on energy transfer, cascade, and destruction. Specifically, SG-CFD involves a) long-range interaction [10]; b) absence of incompressibility; and c) collisionless nature. The long-range interaction requires the formation of halos (the counterpart of vortex) to maximize system entropy [11, 12], a unique and elementary structure of SG-CFD [13, 14]. The lack of incompressibility implies a non-zero velocity divergence. At large scale and in the linear regime, the density fluctuations are directly proportional to velocity divergence that leads to a nonuniform density field. On the halo scale, the highly localized dense halos cannot be severely deformed by tidal effects due to the lack of incompressibility. Finally, while viscous dissipation is the only mechanism to dissipate the kinetic energy and/or destroy the enstrophy, it is not present in collisionless SG-CFD. Energy can only be cascaded and transferred in different forms, but not destroyed.

While inverse mass cascade is not present in hydrodynamic turbulence, it is a key feature of SG-CFD [1] and is highly correlated with energy cascade. There exists a broad spectrum of halo sizes. Halos pass their mass onto larger and larger halos, until mass growth becomes dominant over mass propagation. Consequently, we expect a continuous multistage cascade of mass from smaller to larger mass scales, i.e. “Little halos have big halos, That feed on their mass; And big halos have greater halos, And so on to growth”. Effects of mass cascade on halo mass function



have been studied with new mass function proposed [1]. In addition, effects of mass cascade on halo energy, size and density profile are also discussed with halo density explicitly formulated [2]. This paper focus on the energy cascade of SG-CFD and its relations to mass cascade, along with the effects of halo shape on energy cascade. The rest of paper is organized as follows: Section 2 introduces the simulation used for this work. Section 3 briefly reviews the key formulations of inverse mass cascade, followed by developing the idea of energy cascade into mathematical formulations for SG-CFD in Section 4. The temporal evolution of total kinetic and potential energies in the entire system is also studied. Effects of halo shape change on energy cascade are discussed in Section 5.

## **2. The simulation and numerical data**

The numerical data for this work is publicly available and generated from the  $N$ -body simulations carried out by the Virgo consortium. A comprehensive description of the simulation data can be found in [15, 16]. The same set of simulation data has been widely used in a number of different studies from clustering statistics [16] to the formation of halo clusters in large scale environments [17], and testing models for halo abundance and mass functions [18]. More details can be found in supplementary information.

## **3. Real-space inverse mass cascade of SG-CFD**

The real-space inverse mass cascade of self-gravitating collisionless flow (SG-CFD) has been previously studied [1]. The SG-CFD flow involves a continuous mass and energy cascade across halos on different mass scales, where the energy cascade is intimately related to the mass cascade. This section briefly reviews the key findings of inverse mass cascade. We rely on mass flux function to quantify the net transfer of mass from all halos below a given mass scale  $m_h$  to all

halos above that scale at any time  $t$  (or the scale factor  $a$  or redshift  $z$ ). The mass flux function  $\Pi_m(m_h, a)$  is defined as

$$\Pi_m(m_h, a) = -\frac{\partial}{\partial t} \left[ M_h(a) \int_{m_h}^{\infty} f_M(m, m_h^*) dm \right]. \quad (3)$$

Here  $M_h(a)$  is the total mass in all halos that increases with time, i.e. the total mass of a halo sub-system. By contrast, the total mass  $M_o(a)$  of an out-of-halo sub-system includes all collisionless particles that do not belong to any halos. The halo mass function  $f_M(m_h, m_h^*(a))$  is the probability distribution of total halo mass  $M_h(a)$  with respect to halo mass  $m_h$  (or to the number of particles in halo  $n_p = m_h/m_p$ ), where  $m_p$  is the mass of a single particle (or single merger, the mass resolution of  $N$ -body simulation). The characteristic mass scale  $m_h^*(a)$  (or  $n_p^* = m_h^*/m_p$ ) gives the size of typical halos formed at time  $t$  and increases with time. The mass flux function  $\Pi_m$  should be independent of halo size  $m_h$  for halo groups smaller than  $m_h^*(a)$  (i.e. a mass propagation range), where mass flux function reduces to

$$\varepsilon_m(a) = \Pi_m(m_h, a) \quad \text{for} \quad m_h \ll m_h^*, \quad (4)$$

while flux function  $\Pi_m$  is mass-scale dependent in the mass deposition range.

The constant mass flux (or the mass dissipation rate  $\varepsilon_m$ ) propagates mass from the smallest mass scale to the characteristic scale ( $0 \ll m_h < m_h^*$ ) in the mass propagation range. Here the total mass of a halo group of size  $m_h$  is given by,

$$m_g(m_h, a) = n_h m_h = M_h(a) f_M(m_h, m_h^*) m_p, \quad (5)$$

where  $n_h$  is the number of halos in a halo group including all halos with same mass  $m_h$ .

The real-space mass transfer function  $T_m$  can be defined as the derivative of the mass flux function with respect to halo mass  $m_h$ ,

$$T_m(m_h, a) = \frac{\partial \Pi_m(m_h, a)}{\partial m_h} = \frac{\partial [M_h(a) f_M(m_h, m_h^*)]}{\partial t} = \frac{\partial m_g(m_h, a)}{m_p \partial t}, \quad (6)$$

which quantifies the rate of change of the group mass  $m_g(m_h, a)$ . If we write the mass flux function as the integration of mass transfer function, i.e.

$$\Pi_m(m_h, a) = \int_0^{m_h} T_m(m, a) dm, \quad (7)$$

where  $T_m(m, a)$  clearly represents the rate of mass transfer from halo groups with mass  $m$  below  $m_h$  to halo groups with mass above  $m_h$ . The integration of  $T_m$  is the total rate of mass transfer  $\Pi_m$ . For mass propagation range (Eqs. (4) and (6)),

$$T_m(m_h, a) = 0 \quad \text{and} \quad \frac{\partial m_g(m_h, a)}{\partial t} = 0 \quad \text{for } m_h < m_h^*, \quad (8)$$

where halo group mass  $m_g$  is time-invariant in mass propagation range. The mass transfer function  $T_m(m_h, a)$  describes the removal of mass from a small scale and the deposition of mass at a large scale, where  $T_m(m_h, a) > 0$  when  $m_h > m_h^*$  indicates that mass is deposited to grow halos above the characteristic size  $m_h^*$ .

The scale-independent mass flux  $\varepsilon_m$  leads to a constant group mass  $m_g(m_h) \equiv m_g(m_h, a)$  that reaches a steady state in the propagation range (Eq. (8)). Mass injected at the smallest mass scale is simply propagated through all halo groups below the characteristic size  $m_h^*$  and consumed (deposited) to grow halos above the characteristic mass  $m_h^*$ . Halos below  $m_h^*$  does not grow with time. The mass scale  $m_h^*$  increases with time and extends the propagation range to larger and larger

mass scale. Since mass flux  $\varepsilon_m(a)$  is independent of halo mass if  $m_h < m_h^*$ , the mass flux at the smallest scale reads (Eq. (3) with  $m_h = 0$ )

$$\varepsilon_m(a) = \Pi_m(m_h = 0, a) = -\frac{\partial M_h(a)}{\partial t} = -\left(\frac{3}{2} - \tau_0\right) M_h(a) H \quad \text{if} \quad m_h < m_h^*, \quad (9)$$

where the total halo mass  $M_h(a) \sim a^{3/2 - \tau_0}$  (Table 2 in [1]).

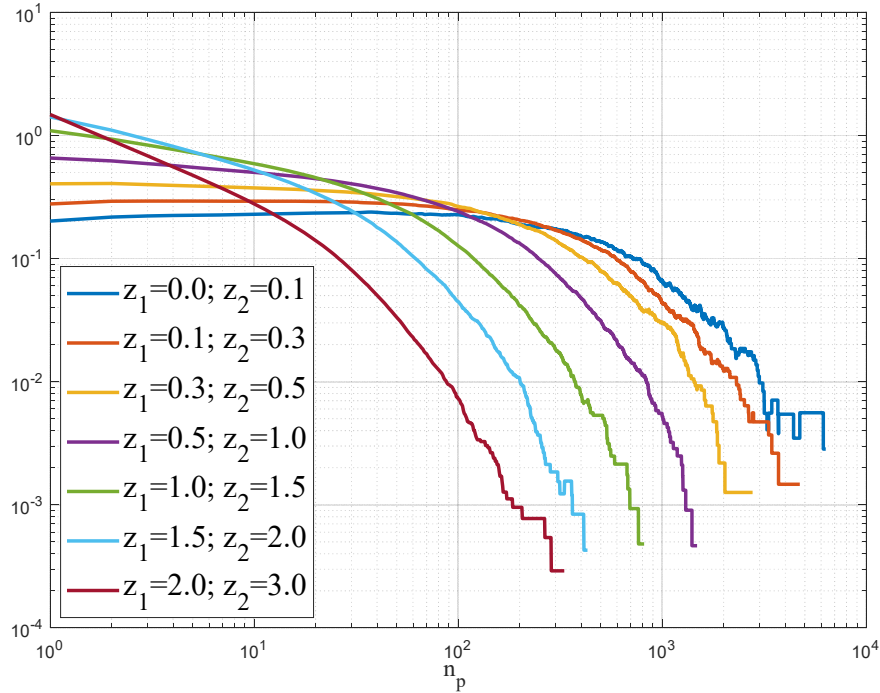


Figure 1. Mass flux function  $-\Pi_m(m, a)$  (normalized by  $Nm_p/t_0$  and  $t_0$  is the current time) computed from simulation results using halo group mass  $m_g(a)$  at two different redshifts  $z$  (Eq. (3)). A scale-independent mass flux  $\varepsilon_m(a)$  can be found for propagation range. The negative mass flux  $\varepsilon_m(a)$  clearly indicates an inverse mass cascade from small to large scales. The mass propagation range (with scale-independent  $\varepsilon_m(a)$ ) is formed at  $z = 0.3$  and extends to larger mass scale with time.

Figure 1 plots the mass flux function  $-\Pi_m(m, a)$  computed from a  $N$ -body simulation using halo group mass  $m_g(a)$  at two different redshifts  $z$  (Eq. (3)). A scale-independent mass flux  $\varepsilon_m(a)$  can be clearly identified in the propagation range ( $m_h < m_h^*$ ). The negative mass flux function  $\varepsilon_m(a) < 0$  indicates an inverse mass cascade from small to large scales. The propagation range is clearly formed at around  $z = 0.3$  and gradually extends to larger and large mass scale with time.

Let time scale  $\tau_h(m_h, a)$  be the average waiting time for a single merging event in a halo group of mass  $m_h$ . The scale-independent rate of mass transfer from scale below  $m_h$  to above  $m_h$  is

$$\varepsilon_m(a) = -m_h / \tau_h(m_h, a) \quad \text{for} \quad m_h \ll m_h^*. \quad (10)$$

Because halo interactions are local in mass space, we can assume the dominant merging events in an infinitesimal time involves merging between a halo and a single merger. This is a fundamental step in mass cascade and explored by a TBCM model (two-body collapse model [19]) that provides more insights than a simple spherical collapse model [20]. The average waiting time  $\tau_g = n_h \tau_h$  (halo lifespan Eq. (5) in [1]) for a halo of mass  $m_h$  is  $\tau_g \propto a^{\tau_0} m_h^{-\lambda}$  (Eq. (45) in [1]), where  $\tau_0 \approx -1$  is usually assumed and  $\lambda$  is a halo geometry parameter. With  $\lambda = 2/3$  for large halos and a constant waiting time  $\tau_g$ , the halo mass  $m_h^L(t) \sim t$ . The actual halo lifespan can be a random variable. Now let's assume a typical halo of mass  $m_h^L(t)$  that is constantly growing with the waiting time exactly to be  $\tau_g$  for every single merging during its entire mass accretion history.

The total halo mass  $M_h(a)$  can be related to the mass of that typical halo  $m_h^L$  as (Eq. (53) in [1]),

$$M_h(a) = \frac{1}{1-\lambda} m_h^L n_h^L n_p^L = \frac{1}{\beta_0} m_h^* n_h^* n_p^*, \quad (11)$$

where  $\beta_0$  is a numerical constant for mass function  $f_M(m_h, m_h^*(a))$ . The scale-independent mass flux  $\varepsilon_m$  can be eventually expressed as (Eq. (54) in [1])

$$\varepsilon_m(a) = -\frac{dm_h^L}{dt} n_h^L n_p^L = -\frac{1}{(1-\lambda)} \frac{d(m_h^L n_h^L n_p^L)}{dt} = -\left(\frac{3}{2} - \tau_0\right) M_h H, \quad (12)$$

where  $n_h^L$  is the number of that typical halos in the halo group of mass  $m_h^L$  and  $n_p^L$  is the number of particles in that typical halo. Here  $n_h^L \sim (m_h^L)^{-(1+\lambda)}$  and decreases with the halo mass  $m_h^L$ .

For hydrodynamic turbulence, the vortex stretching is generally considered as the major mechanism to facilitate the energy transfer from large to small length scales. Vortex stretches into smaller scales with kinetic energy transferred to smaller scales simultaneously. Halos is the building block in SG-CFD. Equation (11) tells us that the entire halo sub-system can be equivalently considered consisting of only typical halos of mass  $m_h^L$  with an equivalent number of halos  $n_h^L n_p^L$ . Equation (12) quantifies the mass flux  $\varepsilon_m$  in terms of the growth of typical halos. Halos constantly merges with single mergers from out-of-halo sub-system, which facilitates the inverse mass cascade from small to large mass scales. It was also shown that (Eq. (50) in [1]) the mass of typical halos and total halo mass scales with  $a$ ,

$$m_h^L(a) \sim a^{\lambda_m} = a^{\frac{3/2-\tau_0}{1-\lambda}} \quad \text{and} \quad M_h(a) \sim a^{(1-\lambda)\lambda_m} \quad \text{with} \quad \lambda_m = \frac{3/2-\tau_0}{1-\lambda}. \quad (13)$$

If  $\tau_0 = 1$  and  $\lambda = 2/3$  (i.e.  $\lambda_m = 3/2$ ), we should have  $m_h^L(a) \sim a^{3/2} \sim t$ ,  $n_h^L n_p^L \sim (m_h^L)^{-\lambda} \sim a^{-1}$  and  $M_h(a) \sim a^{1/2}$ . Typical halos grow at a constant rate with time while the equivalent number of typical halos ( $n_h^L n_p^L$ ) decreases as  $a^{-1}$  such that mass flux function  $\varepsilon_m(a) \sim a^{-1}$  (Eq. (12)).

Just like the mass cascade, the energy cascade can be facilitated by the growth of those typical halos via merging with single mergers. With halos growing from small to large mass scales, the total kinetic energy of that halo increases while potential energy decreases such that energy is cascaded across mass scales. This qualitative picture hints an inverse kinetic energy cascade and a direct potential energy cascade. Quantitative analysis is provided in the next section.

#### 4. Real-space energy cascade of SG-CFD

##### 4.1 Inverse cascade of halo kinetic energy

Individual halos are characterized by the halo size (the number of particles  $n_p$  or equivalently halo mass  $m_h$ ), one-dimensional halo virial dispersion ( $\sigma_v^2$ ), and halo velocity ( $\mathbf{u}_h$ ) (the mean velocity of all particles in that halo). Particle velocity  $\mathbf{u}_p$  can be decomposed into

$$\mathbf{u}_p = \mathbf{u}_h + \mathbf{u}'_p, \quad (14)$$

where  $\mathbf{u}'_p$  is the fluctuation of particle velocity around halo velocity  $\mathbf{u}_h$ . The virial dispersion  $\sigma_{vh}^2$  is the dispersion of fluctuation velocity  $\mathbf{u}'_p$  and defined as

$$\sigma_{vh}^2 = \text{var}(\mathbf{u}'_p^x) = \text{var}(\mathbf{u}'_p^y) = \text{var}(\mathbf{u}'_p^z), \quad (15)$$

i.e. the variance of velocity fluctuation for all particles in the same halo. Virial dispersion  $\sigma_{vh}^2$  represents the mean kinetic energy of particles, i.e. the temperature of that halo.

The halo velocity  $\mathbf{u}_h = \langle \mathbf{u}_p \rangle_h$  is the mean velocity of all particles in the same halo, where  $\langle \rangle_h$  stands for the average for all particles in the same halo. All halos identified in the system can be grouped into halo groups of the same size. Halo groups are characterized by the size of halos in that group ( $n_h$  or  $m_h$ ), the mean halo virial dispersion ( $\sigma_v^2$ ), and the one-dimensional halo velocity

dispersion ( $\sigma_h^2$ ) that is defined as the dispersion (variance) of halo velocity  $\mathbf{u}_h$  for all halos in the same group,

$$\sigma_v^2 = \langle \sigma_{vh}^2 \rangle_g \quad \text{and} \quad \sigma_h^2 = \text{var}(\mathbf{u}_h^x) = \text{var}(\mathbf{u}_h^y) = \text{var}(\mathbf{u}_h^z). \quad (16)$$

The halo velocity dispersion  $\sigma_h^2$  represents the mean kinetic energy of halos, i.e. the temperature of that halo group, while mean virial dispersion  $\sigma_v^2$  is the mean halo temperature with  $\langle \rangle_g$  for the average for all halos in the same group. Note that the statistics defined at the halo group level is the statistics over many replicas (possible states) of halos with the same mass  $m_h$ . Dispersion of particle velocity of all particles in the same group can be decomposed accordingly,

$$\sigma^2 = \sigma_h^2 + \sigma_v^2. \quad (17)$$

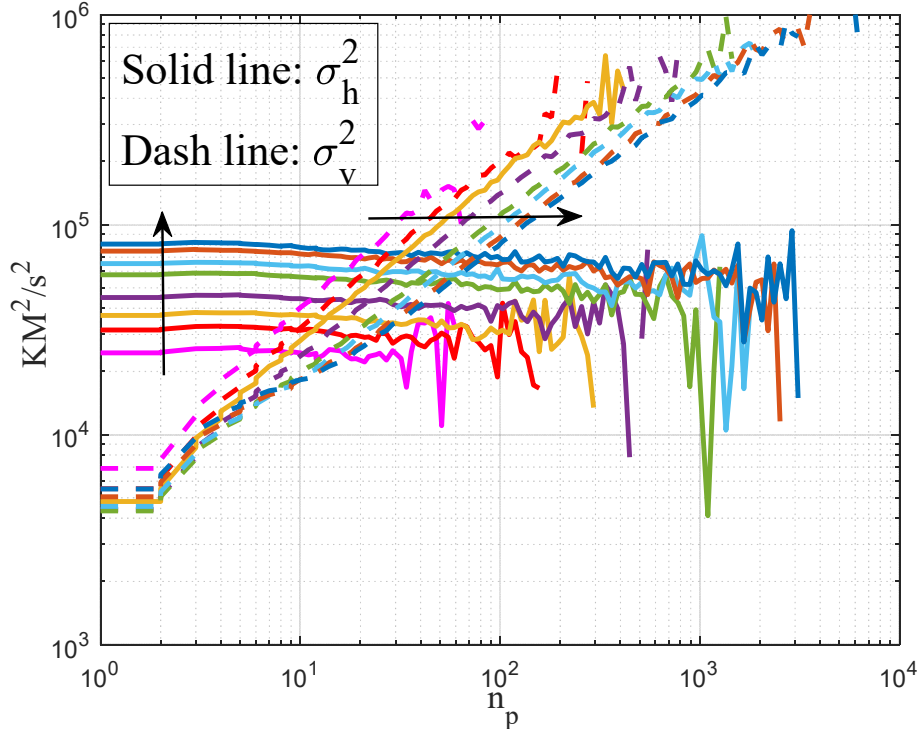


Figure 2. The variation of the halo velocity dispersion  $\sigma_h^2$  (solid lines) and halo virial dispersion  $\sigma_v^2$  (dash lines) with halo group size  $n_p$  for different redshifts  $z = 0, 0.1, 0.3, 0.5, 1.0, 1.5, 2.0,$  and  $3.0$ . Arrows points to the direction of the increasing time or decreasing



redshift  $z$ . The halo velocity dispersion  $\sigma_h^2$  is relatively independent of halo mass and increases with scale factor  $a$ , while halo virial dispersion  $\sigma_v^2$  increases with halo mass and decreases with  $a$  for a given mass.

Figure 2 plots the variation of velocity dispersion  $\sigma_h^2(m_h, a)$  and virial dispersion  $\sigma_v^2(m_h, a)$  with group size  $n_p$  at different redshifts  $z$ . Halo velocity dispersion  $\sigma_h^2$  increases with scale factor  $a$ , while halo virial dispersion  $\sigma_v^2$  decreases with  $a$  for a given size  $m_h$ . The approximate fitting relations are

$$\sigma_h^2(a) \approx \langle \sigma_h^2 \rangle(a) = \beta_{\sigma_h} a u_0^2, \quad (18)$$

$$\sigma_v^2(m_h, a) \approx \beta_{\sigma_v} a^{-1} u_0^2 (m_h/m_p)^{2/3}, \quad (19)$$

with  $\beta_{\sigma_h} = 0.57$  and  $\beta_{\sigma_v} = 0.03$  (see e.g. [21] for other fitting formula), where  $m_p = 2.27 \times 10^{11} M_\odot/h$  (Table S1). Here  $u_0^2$  is the one-dimensional velocity dispersion of the entire system at present epoch ( $z=0$ ) (Table S1 in supplementary information). The virial dispersion of small halos is relatively time-invariant and less dependent on scale factor  $a$  due to their compact stable core structures.

Based on this description, the kinetic energy of a given particle can be separated into two contributions, i.e. halo kinetic energy  $\sigma_h^2$  from the random motion of halos and virial kinetic energy  $\sigma_v^2$  from the particle motion in halos. The halo kinetic energy is dominant for small halos with  $\sigma_h^2 \gg \sigma_v^2$ , while the virial kinetic energy is dominant for large halos  $\sigma_v^2 \gg \sigma_h^2$ . Since mass cascade is facilitated by halo merging with single mergers, it is reasonable to expect that the energy cascade follows a similar way as mass cascade, where the kinetic energy is injected at small scales,

propagated through the mass propagation range, and deposited to grow the kinetic energy of large halos in the mass deposition range.

Here we first focus on the halo kinetic energy  $\sigma_h^2$  and introduce a kinetic energy flux function that quantifies the net transfer of halo kinetic energy  $\sigma_h^2$  from all halos smaller than size  $m_h$  to all halos greater than the size  $m_h$ . Like Eq. (3), kinetic energy flux  $\Pi_{kh}(m_h, a)$  can be defined as

$$\Pi_{kh}(m_h, a) = \underbrace{M_h(a) \int_{m_h}^{\infty} f_M(m, m_h^*) \frac{\partial \sigma_h^2}{\partial t} dm}_1 - \underbrace{\frac{\partial}{\partial t} \left[ M_h(a) \int_{m_h}^{\infty} f_M(m, m_h^*) \sigma_h^2(m, a) dm \right]}_2, \quad (20)$$

where term 2 is the rate of change of the total halo kinetic energy contained in halos greater than  $m_h$ . While the total kinetic energy of a forced steady turbulence is conserved and does not vary with time, the total kinetic energy of SG-CFD does increase with time (more discussion in Section 4.5). Comparing with the mass flux  $\Pi_m(m_h, a)$  in Eq. (3), the extra term (term 1) of  $\Pi_{kh}(m_h, a)$  accounts for the change of halo kinetic energy contained in halos greater than  $m_h$  that is simply due to the time-variation of  $\sigma_h^2(m_h, a)$ , which does not come from the energy cascade and should be excluded. The energy flux after combining two terms together reads

$$\Pi_{kh}(m_h, a) = - \int_{m_h}^{\infty} \frac{\partial}{\partial t} \left[ M_h(a) f_M(m, m_h^*) \right] \sigma_h^2(m, a) dm = - \int_{m_h}^{\infty} T_m(m, a) \sigma_h^2(m, a) dm. \quad (21)$$

The transfer function of halo kinetic energy can be introduced like Eq. (6),

$$T_{kh}(m_h, a) = \frac{\partial \Pi_{kh}}{\partial m_h} = \frac{\partial}{\partial t} \left[ M_h(a) f_M(m_h, m_h^*) \right] \sigma_h^2(m_h, a) = T_m(m_h, a) \sigma_h^2(m_h, a), \quad (22)$$

which is proportional to the mass transfer function  $T_m(m_h, a)$  of mass cascade. Clearly, the energy cascade is intimately related to the mass cascade.

To compute the rate of energy production at the smallest scale, let's introduce the mean rate of energy change

$$\left\langle \frac{\partial \sigma_h^2}{\partial t} \right\rangle = \int_0^\infty f_M(m_h, m_h^*) \frac{\partial \sigma_h^2}{\partial t} dm_h \quad (23)$$

and the mean (specific) halo kinetic energy

$$\langle \sigma_h^2 \rangle = \int_0^\infty f_M(m_h, m_h^*) \sigma_h^2(m_h, a) dm_h. \quad (24)$$

From Eq. (20), the rate of energy production at the smallest scale  $m_h \rightarrow 0$  is

$$\Pi_{kh}(m_h \rightarrow 0, a) = M_h(a) \left\langle \frac{\partial \sigma_h^2}{\partial t} \right\rangle - \frac{\partial}{\partial t} [M_h(a) \langle \sigma_h^2 \rangle]. \quad (25)$$

These expressions can be simplified for a scale-independent halo velocity dispersion, where

$\sigma_h^2(m_h, a) \equiv \langle \sigma_h^2 \rangle(a)$ . The flux function of  $\sigma_h^2$  reads (from Eqs. (18) and (21))

$$\Pi_{kh}(m_h, a) \approx \Pi_m(m_h, a) \langle \sigma_h^2 \rangle, \quad (26)$$

where the energy flux  $\Pi_{kh}$  is proportional to the mass flux  $\Pi_m$ . The rate of energy production at the smallest scale should be (from Eqs. (18) and (25)),

$$\varepsilon_{kh} = \Pi_{kh}(m_h \rightarrow 0, a) = \varepsilon_m \langle \sigma_h^2 \rangle = -\left(\frac{3}{2} - \tau_0\right) M_h(a) H \langle \sigma_h^2 \rangle \quad (27)$$

For  $\tau_0 = 1$ , we have  $M_h(a) \propto a^{1/2}$  and  $\sigma_h^2 \sim a$  from Eq. (18). The rate of energy production  $\varepsilon_{kh}$  should be independent of time and reaches a steady state. Equivalently, the total halo kinetic energy in halo sub-system is proportional to time  $t$  (detail discussion also in Fig. 10).

At the statistically steady state, the mass transfer function  $T_m(m_h, a) \approx 0$  for propagation range (Eq. (8)). The halo kinetic energy flux function  $\Pi_{kh}$  across different size of halos is independent of halo size  $m_h$ , where we have

$$T_{kh}(m_h, a) = 0 \quad \text{and} \quad \varepsilon_{kh}(a) = \Pi_{kh}(m_h, a) \quad \text{for} \quad m_h < m_h^*, \quad (28)$$

which is simply the rate of production of halo kinetic energy at the smallest scale. We can similarly define the total halo kinetic energy in a halo group of same size halos,

$$\sigma_{hg}^2(m_h, a) = M_h(a) f_M(m_h, m_h^*) \sigma_h^2(m_h, a) = \sigma_h^2(m_h, a) m_g(m_h, a) / m_p, \quad (29)$$

The rate of change of which is,

$$\frac{\partial \sigma_{hg}^2}{\partial t} = \frac{\partial m_g(m_h, a)}{\partial t} \frac{\sigma_h^2(m_h, a)}{m_p} + \frac{m_g}{m_p} \frac{\partial \sigma_h^2(m_h, a)}{\partial t}. \quad (30)$$

A direct result of a scale-independent mass flux through halos of different mass scales is a time-invariant group mass  $m_g$  such that,

$$\frac{\partial \sigma_{hg}^2}{\partial t} = \frac{m_g}{m_p} \frac{\partial \sigma_h^2(m_h, a)}{\partial t} \quad \text{for} \quad m_h \ll m_h^*, \quad (31)$$

i.e. the change of  $\sigma_{hg}^2$  in propagation range is only due to the time variation of  $\sigma_h^2$ . The energy cascade simply propagates (not changes) halo kinetic energy through halos in propagation range.

Figure 3 plots the variation of flux function  $-\Pi_{kh}(m_h, a)$  of halo kinetic energy  $\sigma_h^2$  with the halo group size  $n_p$ . The flux function  $\Pi_{kh}$  is negative indicating an inverse cascade from small to large mass scales. The flux function  $\Pi_{kh}$  is numerically computed from simulation results at two different redshifts  $z_1$  and  $z_2$  using Eqs. (20) or (21). A scale-independent flux function  $\varepsilon_{kh}$  can be identified for the mass propagation range with  $m_h < m_h^*$ .

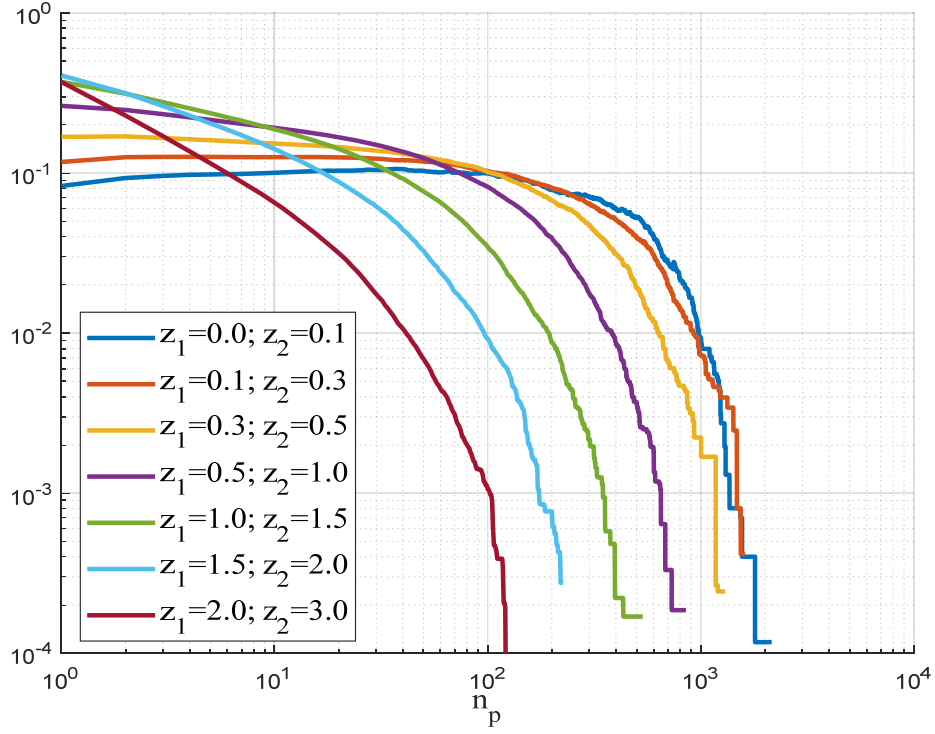


Figure 3. The variation of energy flux function  $-\Pi_{kh}$  for halo kinetic energy  $\sigma_h^2$  with the size  $n_p$  of halo groups. The flux function  $\Pi_{kh} < 0$  (inverse cascade from small to large scales) and is normalized by  $Nm_p u_0^2 / t_0$ . The flux function  $\Pi_{kh}$  is computed from simulation results at two different redshifts  $z_1$  and  $z_2$ . A scale-independent flux function  $\varepsilon_{kh} = \Pi_{kh}(m_h, a)$  can be identified for the mass propagation range with  $m_h < m_h^*$ .

#### 4.2 A general formulation for cascade of a specific quantity

In principle, the flux function for any specific quantity  $V_s$  (an extensive quantity per unit mass) can be similarly derived. For example, let us assume a generic specific variable  $V_s(m_h, a)$  that can be expressed in a general form via separation of variables,

$$V_s(m_h, a) = a^s F_v(m_h), \quad (32)$$

where  $s$  is an arbitrary exponent. The flux function of  $V_s$  can be written as (From Eq. (21)),

$$\Pi_{vs}(m_h, a) = -\int_{m_h}^{\infty} T_m(m, a) V_s(m, a) dm, \quad (33)$$

while the transfer function  $T_{vs}$  of quantity  $V_s$  is proportional to mass transfer function  $T_m$ ,

$$T_{vs}(m_h, a) = T_m(m_h, a) V_s(m_h, a). \quad (34)$$

The rate of production for specific variable  $V_s$  reads (from Eqs. (20) and (25))

$$\varepsilon_{vs} = \Pi_{vs}(m_h \rightarrow 0, a) = M_h(a) \left\langle \frac{\partial V_s}{\partial t} \right\rangle - \frac{\partial}{\partial t} [M_h(a) \langle V_s \rangle], \quad (35)$$

where the mean rate of change for quantity  $V_s$

$$\left\langle \frac{\partial V_s}{\partial t} \right\rangle = \int_0^\infty f_M(m_h, m_h^*) \frac{\partial V_s}{\partial t} dm_h \quad (36)$$

and the mean (specific) variable  $V_s$

$$\langle V_s \rangle = \int_0^\infty f_M(m_h, m_h^*) V_s dm_h. \quad (37)$$

With the general expression for  $V_s$  in Eq. (32), we should have

$$\left\langle \frac{\partial V_s}{\partial t} \right\rangle = sH \langle V_s \rangle \quad (38)$$

from definition (36) and (37). The rate of production for  $V_s$  at the smallest scale is (Eq. (35))

$$\varepsilon_{vs} = -M_h(a) H \langle V_s \rangle \left[ -s + \frac{\partial \ln [M_h(a) \langle V_s \rangle]}{\partial \ln a} \right], \quad (39)$$

or equivalently (using Eq. (9)),

$$\varepsilon_{vs} = \frac{\varepsilon_m \langle V_s \rangle}{3/2 - \tau_0} \left[ -s + \frac{\partial \ln [M_h(a) \langle V_s \rangle]}{\partial \ln a} \right] = \frac{\varepsilon_m \langle V_s \rangle}{3/2 - \tau_0} \left[ \frac{\partial \ln \langle V_s \rangle}{\partial \ln a} - s + \frac{3}{2} - \tau_0 \right]. \quad (40)$$

Clearly, the flux function of any specific quantity is proportional to the flux of mass multiplied by

the mean of that quantity in halo sub-system, i.e.  $\varepsilon_{vs} \sim \varepsilon_m \langle V_s \rangle$ . A scale-independent mass flux  $\varepsilon_m$

will lead to a scale-independent flux  $\varepsilon_{vs}$  of any specific quantity  $V_s$ . By setting  $V_s = \sigma_h^2$  and  $s = 1$

, the flux function of halo kinetic energy  $\varepsilon_{kh}$  (Eq. (27)) can be easily recovered from Eq. (40) .

Since mass cascade can be quantitatively described by the growth of typical halos (Eq. (12)),

similar treatment can be done for the specific quantity  $V_s$  . If we assume a power law for the mean

quantity  $\langle V_s \rangle \sim a^{\lambda_v}$  and  $m_h^L \sim a^{\lambda_m}$  (Eq. (13)), the flux function of quantity  $V_s$  can be directly

written as (from Eqs. (40), (11) and (12)),

$$\varepsilon_{vs} = -\frac{\lambda_v - s + 3/2 - \tau_0}{(\lambda_m + \lambda_v)(1 - \lambda)} \frac{d(m_h^L \langle V_s \rangle)}{dt} n_h^L n_p^L, \quad (41)$$

or

$$\varepsilon_{vs} = \left( \frac{s}{\lambda_v + 3/2 - \tau_0} - 1 \right) \frac{d(M_h \langle V_s \rangle)}{dt} = -(\lambda_v + 3/2 - \tau_0 - s) M_h H \langle V_s \rangle, \quad (42)$$

where the flux function of  $V_s$  can be conveniently related to the rate of change of total quantity

$M_h \langle V_s \rangle$  in all halos. It is very often that  $\lambda_v = 1$  such that the flux function  $\varepsilon_{vs}$  is constant of time.

One step further, if the quantity  $V_s^L \equiv V_s(m_h^L, a)$  for typical halos of mass  $m_h^L$  can be determined,

an equivalent number of typical halos  $N_h^L$  in halo sub-system can be defined as (from Eq. (42)),

$$N_h^L = \frac{M_h \langle V_s \rangle}{m_h^L V_s^L} = \frac{n_h^L n_p^L \langle V_s \rangle}{1 - \lambda V_s^L}, \quad (43)$$

such that  $M_h \langle V_s \rangle = N_h^L m_h^L V_s^L$ , where  $V_s^L$  is the specific quantity  $V_s$  for a typical halo. Now the flux

function for the cascade of any quantity  $V_s$  can be directly related to the mass accretion of the

typical halo from Eq. (42),

$$\varepsilon_{vs} = -\frac{\lambda_v - s + 3/2 - \tau_0}{(\lambda_m + \lambda_v - \lambda \lambda_m)} \frac{d(m_h^L N_h^L V_s^L)}{dt} = -(\lambda_v + 3/2 - \tau_0 - s) H m_h^L N_h^L V_s^L. \quad (44)$$

Examples of the specific quantity  $V_s^L$  can be halo specific kinetic/potential energies and radial/rotational kinetic energies from coherent motion. For example, the virial kinetic energy of a typical halo is  $\sigma_v^2(m_h^L, a) \sim a^{-1}(m_h^L)^{2/3} \sim a^0$  (from Eq. (19)) that should be time-variant for  $m_h^L \sim a^{3/2}$ . The equivalent number of halos  $N_h^L$  is on the order of  $\sim 10^4$  with both  $n_h^L \sim 100$  and  $n_p^L \sim 100$ . Equation (44) can be conveniently used to estimate the flux function of any quantity. A good examples is for the rotational kinetic energy discussed in Section 4.6 (Fig. 18).

In Hydrodynamic turbulence, the vortex stretching along its axis of rotation facilitates a direct energy cascade from large to small length scales. Similar for SG-CFD, Eq. (44) tells us that the mass accretion of typical halos (the counterpart of vortex) facilitates the cascade of any specific quantity  $V_s$  from small to large mass scales.

### 4.3 Inverse cascade of virial kinetic energy

Next, the general formulation can be used to formulate the cascade of halo virial energy  $\sigma_v^2$ .

The flux function of halo virial energy  $\sigma_v^2$  is first obtained from Eq. (21),

$$\Pi_{kv}(m_h, a) = -\int_{m_h}^{\infty} T_m(m, a) \sigma_v^2(m, a) dm. \quad (45)$$

Unlike the flux function  $\Pi_{kh} \approx \varepsilon_m \sigma_h^2(a)$  for halo kinetic energy  $\sigma_h^2$  in Eq. (27),

$\Pi_{kv} \neq \varepsilon_m \sigma_v^2(m_h, a)$  because of the mass-scale dependence of the virial energy  $\sigma_v^2$  (Eq. (19)). The transfer function of virial kinetic energy can be introduced similarly (Eq. (22)),

$$T_{kv}(m_h, a) = T_m(m_h, a) \sigma_v^2(m_h, a). \quad (46)$$

The rate of production of halo virial energy at the smallest scale can be obtained from Eq. (40),



$$\varepsilon_{kv} = \Pi_{kv}(m_h \rightarrow 0, a) = \frac{\varepsilon_m \langle \sigma_v^2 \rangle}{3/2 - \tau_0} \left[ 1 + \frac{\partial \ln [M_h(a) \langle \sigma_v^2 \rangle]}{\partial \ln a} \right]. \quad (47)$$

If the mean halo virial kinetic energy  $\langle \sigma_v^2 \rangle \sim a$ , i.e. the same scaling with  $a$  as the halo kinetic energy  $\langle \sigma_h^2 \rangle$  in Eq. (18), we will finally have (using Eqs. (47) and (12)),

$$\varepsilon_{kv} = \left( 1 + \frac{2}{3/2 - \tau_0} \right) \varepsilon_m \langle \sigma_v^2 \rangle = - \left( \frac{7}{2} - \tau_0 \right) M_h(a) H \langle \sigma_v^2 \rangle. \quad (48)$$

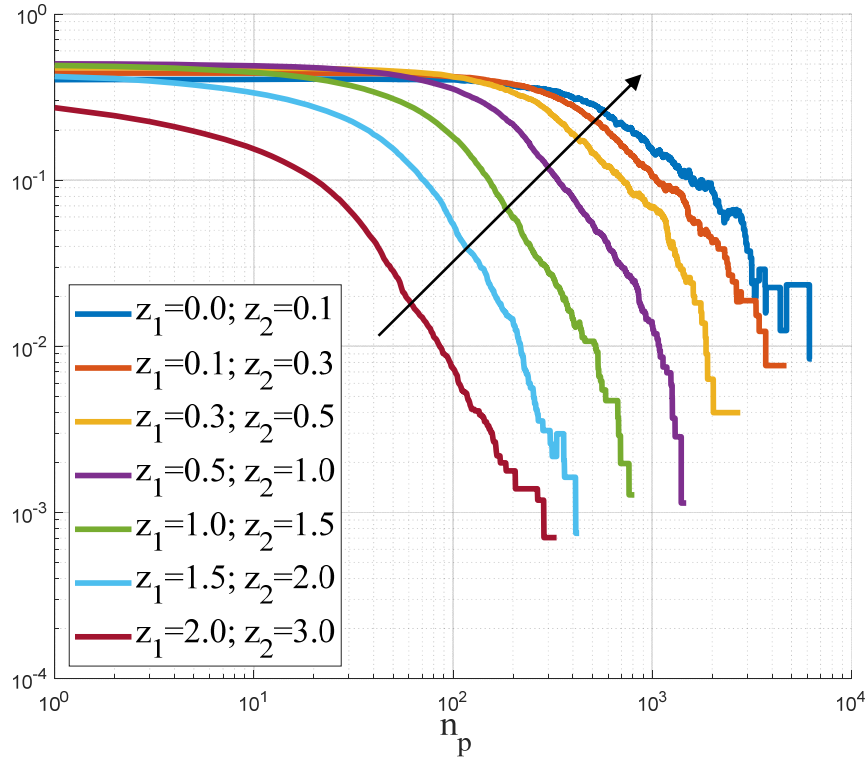


Figure 4. The variation of flux function  $-\Pi_{kv}(m_h, a)$  for halo virial energy  $\sigma_v^2(m_h)$  with the size  $n_p$  of halo groups. The flux function  $\Pi_{kv} < 0$  (inverse cascade from small to large scales) and is normalized by  $Nm_p u_0^2 / t_0$ . The flux function  $\Pi_{kv}$  is computed from simulation results at two different redshifts  $z_1$  and  $z_2$ . A scale-independent flux function  $\varepsilon_{kv}$  can be identified for mass propagation range with  $m_h < m_h^*$ .

Figure 4 presents the variation of flux function  $-\Pi_{kv}$  with group size  $n_p$  that is computed using simulation data at two different redshifts. The negative value of  $\Pi_{kv}$  indicates an inverse cascade of virial kinetic energy. There is also a scale-independent flux  $\varepsilon_{kv}$  for small halos in mass propagation range. The virial kinetic energy decreases with time for a given size of halo ( $\sigma_v^2$  decreases with time in Eq. (19) with  $s = -1$ ), while the halo kinetic energy increases with time with  $s = 1$  for  $\sigma_h^2$  in Eq. (18). The flux function  $\varepsilon_{kv} \approx 5/(3 - 2\tau_0)\varepsilon_{kh}$  (Eqs. (27) and (48)), while the total amount of two kinetic energies in all halos are comparable with  $\langle \sigma_v^2 \rangle \approx \langle \sigma_h^2 \rangle$  (Fig. 10) after the statistically steady state is established.

#### 4.4 Direct cascade of halo potential energy

The potential energy of halos can be similarly separated into two contributions: i) the potential  $\phi_h(m_h, a)$  due to inter-halo interactions between particles from different halos, and ii) the potential  $\phi_v(m_h, a)$  due to intra-halo interactions between particles from the same halo. To better understand two different potentials, let's first write the gravitational potential energy of a single particle that has two separate contributions (see decomposition of velocity dispersion in Eq. (17)),

$$m_p \phi_i = \frac{1}{2} \sum_{j \neq i}^N V(r_{ji}) = \phi_{iv} + \phi_{ih}, \quad (49)$$

with two separate contributions written as

$$\phi_{iv} = \frac{1}{2} \sum_{k \neq i}^{n_p} V(r_{ki}) \quad \text{and} \quad \phi_{ih} = \frac{1}{2} \sum_l^{N-n_p} V(r_{li}), \quad (50)$$

respectively, where  $N$  is the total number of particles in the system,  $\phi_i$  is the specific potential of particle  $i$ ,  $r_{ji}$  is the distance between two particles  $j$  and  $i$ , and  $V(r_{ji})$  is the gravitational potential.

The first term  $\phi_{iv}$  is the intra-halo potential from pair interactions with all other particles in the same halo of size  $n_p$ . The second term  $\phi_{ih}$  is the inter-halo potential from pair interactions with all other particles (denoted as particle  $l$ ) out of the halo that particle  $i$  resides in. Halos are small when compared to the typical separation between halos. Any two particles  $i$  and  $j$  in the same halo should have a distance  $r_{ij} \ll r_{li} \approx r_{lj}$ , where intra-halo distance is much smaller than the inter-halo distance to particle  $l$  from a different halo. Therefore, particles in the same halo should have a similar background potential ( $\phi_{ih} \approx \phi_{jh}$ ).

The inter- and intra- halo potentials for individual halos are defined as the average of particle potentials for all  $n_p$  particles in the same halo,

$$\phi_{hv} = \langle \phi_{iv} \rangle_h = \frac{1}{n_p} \sum_{i=1}^{n_p} \phi_{iv} \quad \text{and} \quad \phi_{hh} = \langle \phi_{ih} \rangle_h = \frac{1}{n_p} \sum_{i=1}^{n_p} \phi_{ih} \approx \phi_{ih}. \quad (51)$$

Finally, the inter- and intra- halo potentials for halo groups are defined as the average of all  $n_h$  halos in the same group, i.e.

$$\phi_v(m_h, a) = \langle \phi_{iv} \rangle_g = \frac{1}{n_h} \sum_{i=1}^{n_h} \phi_{iv} \quad \text{and} \quad \phi_h(m_h, a) = \langle \phi_{ih} \rangle_g = \frac{1}{n_h} \sum_{i=1}^{n_h} \phi_{ih}. \quad (52)$$

Halo mass is small compared to the system mass ( $m_h \ll M$  or  $n_p \ll N$ ), such that the number of particles (particle  $l$  in Eq. (50)) out of any halo is about the same for all different halos. Therefore, we expect the inter-halo potential  $\phi_h$  for a halo group to be much less dependent on the halo size  $m_h$  or  $n_p$  in contrast to the intra-halo potential  $\phi_v$  that is strongly dependent on halo size  $m_h$ . At large scale, halos can be considered as macro-particles with a relatively homogeneous spatial distribution. The inter-halo potential  $\phi_h$  should be relatively independent on both position and mass due to the spatial homogeneity. Hence,  $\phi_h$  may be considered as a background potential.

Figure 5 plots the variation of intra-halo potential ( $\phi_v$ :dash lines) and inter-halo potential ( $\phi_h$ :solid lines) with the halo group size  $n_p$  at different redshifts  $z$ . As expected, the inter-halo potential  $-\phi_h \sim a$  is relatively independent of the halo size, while intra-halo potential  $\phi_v$  scales as  $-\phi_v \sim a^{-1}m_h^{2/3}$  for large halos.

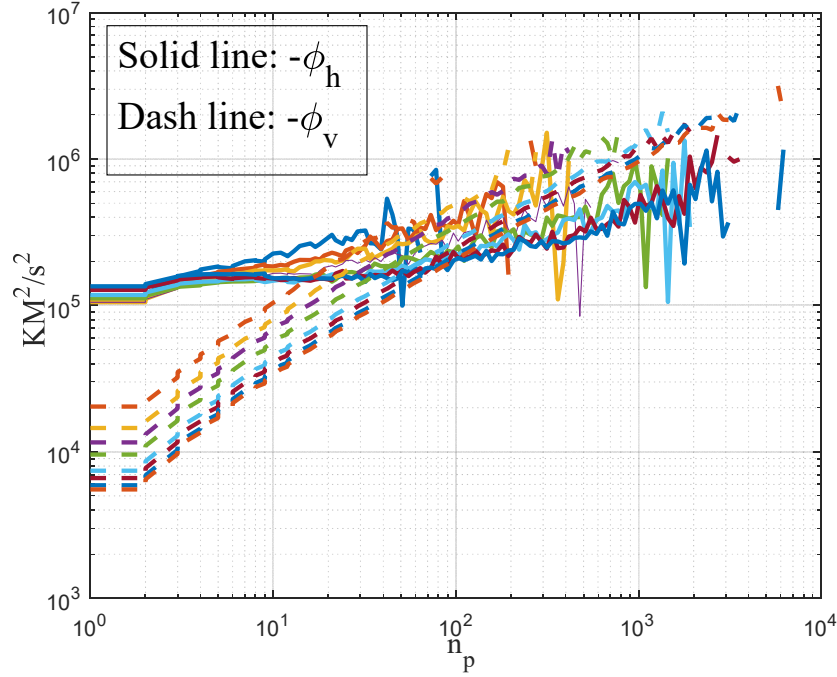


Figure 5. The variation of inter-halo potential  $\phi_h(m_h, a)$  and intra-halo potential  $\phi_v(m_h, a)$  with halo group size  $n_p$  for different redshifts  $z = 0, 0.1, 0.3, 0.5, 1.0, 1.5, 2.0,$  and  $3.0$ . The inter-halo potential  $-\phi_h \sim a$  is relatively independent of the halo size, while inter-halo potential  $\phi_v$  scales as  $-\phi_v \sim a^{-1}m_h^{2/3}$  for large halos.

The virial equilibrium for halo groups can be checked by the virial ratios defined as

$$\gamma_v = -3\sigma_v^2/\phi_v \quad \text{and} \quad \gamma_h = -3\sigma_h^2/\phi_h \quad (53)$$

for motion in halos and motion of halos. Figure 6 plots the variation of two virial ratios  $\gamma_h$  and  $\gamma_v$  with halo group size  $n_p$ . For random motion of halos,  $\gamma_h$  approaches a constant value around 2 for  $n_p = 1$  (out-of-halo sub-system) and decreases with halo size. While for motion in halo,  $\gamma_v$

approaches a constant value between 1.3 and 1.4. This is due to the mass cascade and halo surface energy (see effective potential exponent  $n_e$  in Eq. (96) of [2]).

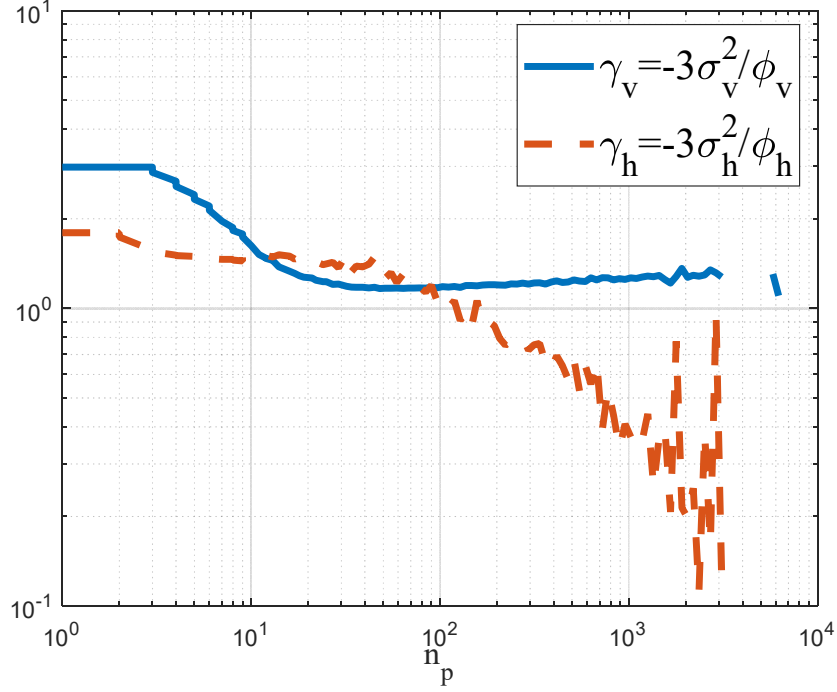


Figure 6. The variation of two virial ratios  $\gamma_h$  and  $\gamma_v$  with the halo group size  $n_p$  for redshift  $z = 0$ . For random motion of halos, the ratio  $\gamma_h$  approaches a constant value around 2 for  $n_p = 1$  (out-of-halo sub-system). For motion of particles in halos, the virial ratio  $\gamma_v$  approaches a constant value between 1.3 and 1.4 for large halos. Note that there might be a greater uncertainty for ratio  $\gamma_h$  for large halos due to fewer number of large halos available in the system for a reliable statistics. Both ratios should be one if the virial theorem is exactly satisfied. The deviation of  $\gamma_v$  is due to the halo surface energy (discussed in [2]).

There might be a greater uncertainty of  $\gamma_h$  for large halos because of fewer number of large halos available for a reliable statistics. Both virial ratios should be 1 if virial theorem is exactly satisfied. Similarly, the flux function of inter- and intra- potential energies are (Eq. (39))

$$\varepsilon_{\phi_h} = \Pi_{\phi_h}(m_h \rightarrow 0, a) = \varepsilon_m \langle \phi_h \rangle = -\left(\frac{3}{2} - \tau_0\right) M_h(a) H \langle \phi_h \rangle, \quad (54)$$

$$\varepsilon_{\phi_v} = \Pi_{\phi_v}(m_h \rightarrow 0, a) = \frac{\varepsilon_m \langle \phi_v \rangle}{3/2 - \tau_0} \left[ 1 + \frac{\partial \ln[-M_h(a) \langle \phi_v \rangle]}{\partial \ln a} \right]. \quad (55)$$

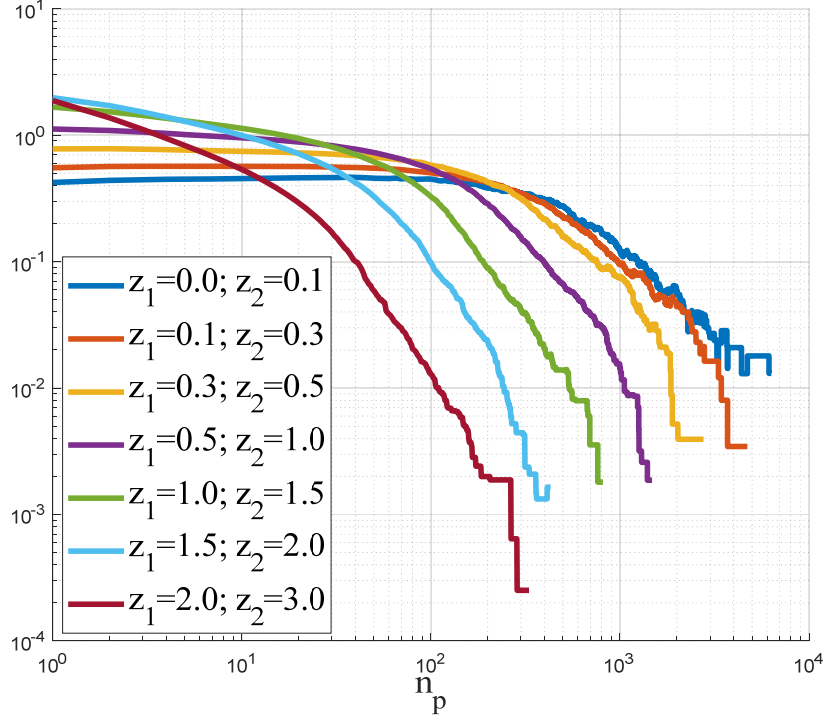


Figure 7. The variation of flux function  $\Pi_{\phi_h}$  of the inter-halo potential energy  $\phi_h(m_h, a)$  with the size  $n_p$  of halo groups. The flux function  $\Pi_{\phi_h} > 0$  (direct cascade from large to small mass scales) and is normalized by  $Nm_p u_0^2 / t_0$ . A scale-independent flux function  $\varepsilon_{\phi_h}$  can be identified for mass propagation range with  $m_h < m_h^*$ .

Figures 7 and 8 plot the variation of flux functions  $\Pi_{\phi_h}$  and  $\Pi_{\phi_v}$  for inter- and intra-halo potential energies, respectively. Both potential energies have a positive flux function indicating a direct cascade of potential energies, i.e. potential energy decreases (increases in absolute value) with halo growing from small to large mass scales. This can be shown from Eqs. (54) and (55), where  $\varepsilon_m < 0$  and mean potential  $\langle \phi_h \rangle < 0$  and  $\langle \phi_v \rangle < 0$ . Since both  $\langle \phi_h \rangle$  and  $\langle \phi_v \rangle$  can be dependent on  $\langle \sigma_h^2 \rangle$  and  $\langle \sigma_v^2 \rangle$  through virial theorem (Eq. (53)), the cascade of potential and kinetic energy are related

to each other. The direct cascade of potential energy to the smallest mass scale provides energy flux for the inverse cascade of kinetic energy through halos.

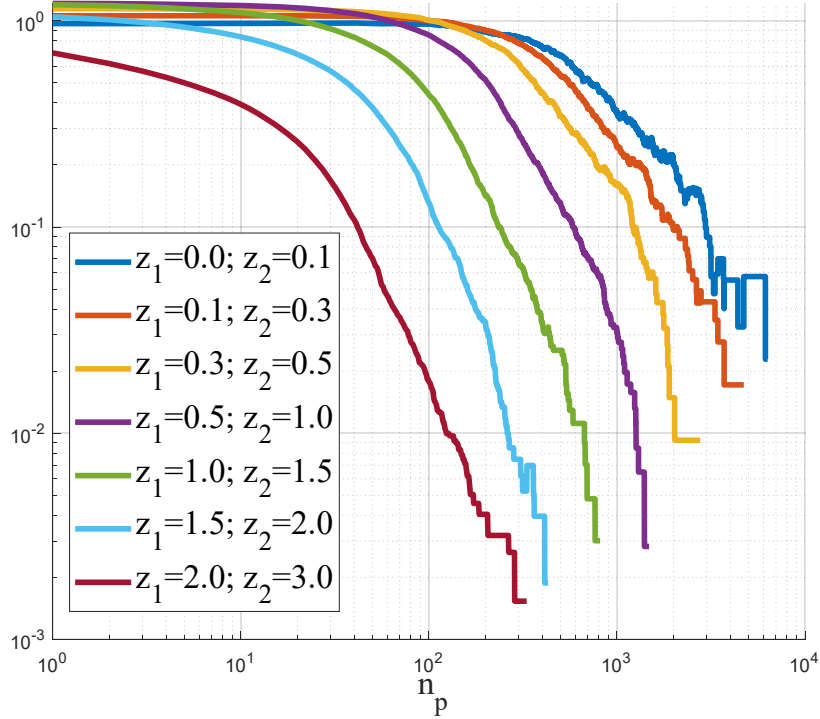


Figure 8. The variation of flux function  $\Pi_{\phi_v}$  of the intra-halo potential energy  $\phi_v(m_h, a)$  with size  $n_p$  of halo groups. The flux function  $\Pi_{\phi_v} > 0$  (direct cascade from large to small mass scales) and is normalized by  $Nm_p u_0^2 / t_0$ . A scale-independent flux function  $\varepsilon_{\phi_v}$  can be identified for mass propagation range with  $m_h < m_h^*$ .

#### 4.5 The temporal evolution of total kinetic and potential energies

In forced steady turbulence, the total mass is conserved, and total kinetic energy of the entire system is also conserved. Kinetic energy is injected at integral scale (the largest scale where external force is applied) and dissipated at the smallest scale (Kolmogorov scale) by molecular viscosity. However, the energy evolution in SG-CFD is much more complicated involving increasing kinetic and potential energies and virilization in halos. The total mass of all halos  $M_h(a)$  also continuously increases due to the inverse mass cascade.

Here we first divide entire system into a halo sub-system with a total mass of  $M_h(a)$  and an out-of-halo sub-system with a total mass of  $M_o(a)$ . In simulation, halos are identified by a FoF algorithm with the smallest halo containing at least two particles. The total halo mass  $M_h(a)$  includes mass of all particles from all halos. The total mass  $M_o(a)$  of out-of-halo sub-system includes mass of all particles that does not belong to any halos. Second, the kinetic and potential energies for a halo sub-system can be decomposed on two different levels: i) halo kinetic energy  $\langle \sigma_h^2 \rangle$  and inter-halo potential  $\langle \phi_h \rangle$  for random motion of halos, and ii) virial kinetic energy  $\langle \sigma_v^2 \rangle$  and intra-halo potential  $\langle \phi_v \rangle$  for particle motion in halos. For out-of-halo sub-system, the mean kinetic energy  $\langle \sigma_{ho}^2 \rangle$  and potential energy  $\langle \phi_{ho} \rangle$  can also be correspondingly computed with all out-of-halo particles identified. Here  $\langle \bullet \rangle$  stands for the average of a quantity over all particles in respective sub-systems.

Figure 9 plots the variation of  $M_h(a)$  and  $M_o(a)$  with scale factor  $a$ . A continuous mass exchange ( $M_o$  decreases while  $M_h$  increases with  $a$ ) between two sub-systems is required to sustain the growth of total halo mass as  $M_h(a) \sim a^{1/2}$  once the statistically steady state is established. The virial equilibrium for two sub-systems at two different levels of particle motion are also checked using virial ratios defined before (Eq. (53)).



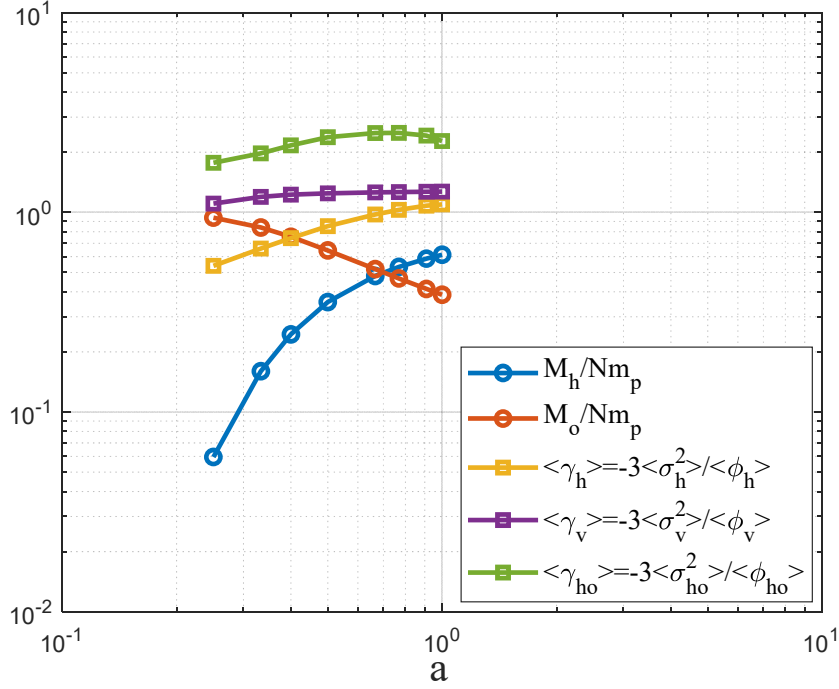


Figure 9. The variation of halo mass  $M_h(a)$  and out-of-halo mass  $M_o(a)$  with scale factor  $a$ . A continuous mass exchange between two sub-systems is required to sustain the total halo mass growing as  $M_h(a) \sim a^{1/2}$  after reaching the statistically steady state. The variation of virial ratios for two sub-systems are also presented. For the motion of halos, the ratio  $\langle \gamma_h \rangle$  (yellow) slowly increases from 0.5 to 1 and it takes longer time to reach virial equilibrium. The ratio  $\langle \gamma_v \rangle \sim 1.3$  (purple) for particle motion within individual halos is relatively time-invariant and the virial equilibrium is established much faster in individual halos. The deviation of  $\langle \gamma_v \rangle$  from 1 reflects the effects of halo mass accretion and halo surface energy [2]. The virial ratio  $\langle \gamma_{ho} \rangle \approx 2$  (green) for out-of-halo particles indicating that the out-of-halo sub-system is energy conserved (no virialization).

At the halo level,  $\langle \gamma_h \rangle$  slowly increases from  $\sim 0.5$  to  $\sim 1$  and the motion of halos takes longer time to reach virial equilibrium. For particle motion in halos, the virial ratio  $\langle \gamma_v \rangle \sim 1.3$  is relatively time-invariant. The virial equilibrium is established much faster and earlier for particle motion in individual halos. The deviation of  $\langle \gamma_v \rangle$  from 1 reflects the effects of halo mass accretion and halo surface energy [2]. The virial ratio  $\langle \gamma_{ho} \rangle \sim 2$  for an out-of-halo particles indicates that the out-of-

halo sub-system is energy conserved (no virilization and kinetic energy always cancels potential energy) with  $3\langle\sigma_{ho}^2\rangle/2 + \langle\phi_{ho}\rangle \approx 0$ .

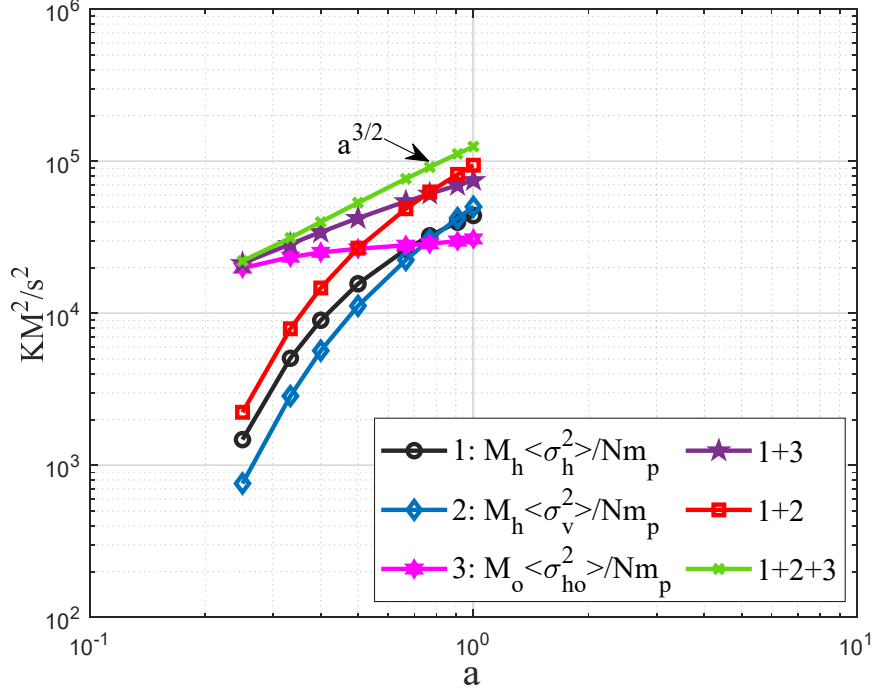


Figure 10. The variation of three kinetic energies with scale factor  $a$ , i.e. halo kinetic energy (1:  $\langle\sigma_h^2\rangle$  black), virial kinetic energy (2:  $\langle\sigma_v^2\rangle$  blue), and out-of-halo kinetic energy (3:  $\langle\sigma_{ho}^2\rangle$  magenta). The total kinetic energy of the entire system (green line: 1+2+3) grows approaching the scaling  $a^{3/2}$ . The kinetic energy of out-of-halo sub-system (magenta: 3) is relatively time-invariant. The total kinetic energy of halo sub-system (red: 1+2) becomes dominant over out-of-halo sub-system with  $M_h(a) \sim a^{1/2}$ ,  $\langle\sigma_h^2\rangle \sim a$ , and  $\langle\sigma_v^2\rangle \sim a$ . A cross-over can be found at around  $a=0.5$ .

Figure 10 illustrates the variation of three kinetic energies with scale factor  $a$ . The total kinetic energy of two sub-systems (green line: 1+2+3, i.e. the one-dimensional velocity dispersion  $u^2$ ) grows approaching the scaling  $\sim a^{3/2}$  or  $\sim t$  (corresponding to a constant energy flux function). The total kinetic energy of out-of-halo sub-system (magenta: 3) is relatively time-invariant and does not change with time. The total kinetic energy of out-of-halo sub-system is conserved while total

mass  $M_o$  decreases with time. The kinetic energy of halo sub-system (red: 1+2) becomes dominant over the out-of-halo sub-system with  $M_h(a) \sim a^{1/2}$ ,  $\langle \sigma_h^2 \rangle \sim a$ , and  $\langle \sigma_v^2 \rangle \sim a$ . A cross-over can be found at around  $a=0.5$ .

Similarly, Fig. 11 shows the variation of three potential energies with scale factor  $a$ . The total potential energy of two sub-systems (green line: 1+2+3) also grows as  $a^{3/2}$ . The out-of-halo sub-system has a time-invariant potential energy (magenta: 3). The potential energy from halo sub-system (red: 1+2) becomes dominant after  $a=0.5$ .

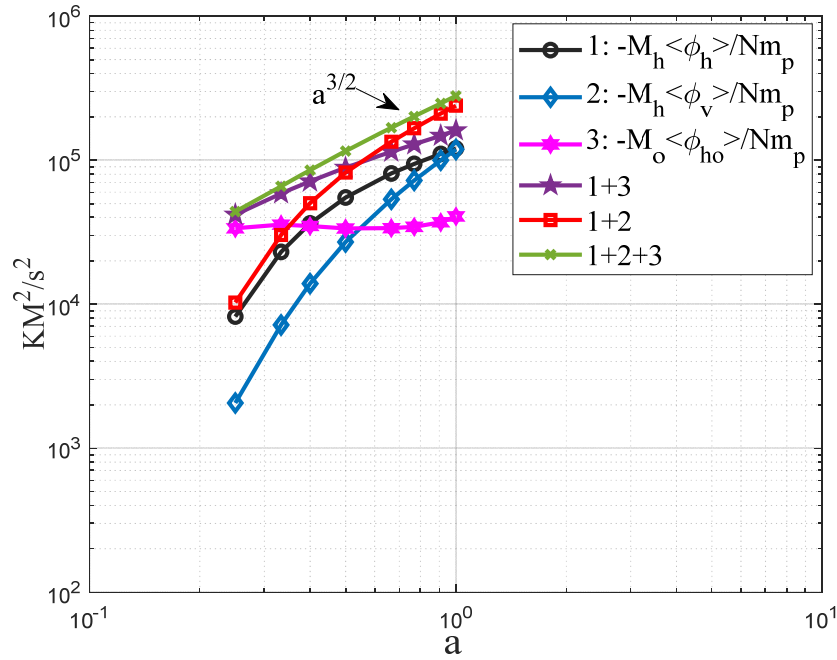


Figure 11. The variation of three potential energies with the scale factor  $a$ , i.e. inter-halo potential (1:  $\langle \phi_h \rangle$  black), intra-halo potential (2:  $\langle \phi_v \rangle$  blue), and potential of out-of-halo particles (3:  $\langle \phi_{ho} \rangle$  magenta). The total potential energy of two sub-systems (green line: 1+2+3) grows as  $a^{3/2}$ . The out-of-halo sub-system has a relatively time-invariant potential energy (magenta: 3). The potential energy from halo sub-system (red: 1+2) becomes dominant with increasing halo mass  $M_h(a) \sim a^{1/2}$ .

To summarize, there is a net mass flux into the halo sub-system to sustain the continuous growth of halo mass. However, the out-of-halo sub-system is energy conserved at any time, i.e.

the total energy of out-of-halo sub-system (sum of potential and kinetic energy) is always nearly zero with a virial ratio  $\gamma_h \approx 2$ . The energy change of the entire system purely comes from the virilization in halo sub-system. The kinetic and potential energies of single mergers (particles in out-of-halo system) always cancel out. The inverse cascade of mass is accompanied by an inverse cascade of kinetic energy and a direct cascade of potential energy. Two energy cascades are related by the virial ratios. The total kinetic and potential energies (absolute value) of halo sub-system increase linearly with time  $t$  when the statistically steady state is established, i.e. a constant energy flux into halo sub-system.

#### 4.6 Inverse cascade of halo radial and rotational kinetic energy

In hydrodynamic turbulence, the production of turbulence kinetic energy is facilitated through the Reynolds stress, a fictitious stress arising from velocity fluctuations to account for the effect of turbulence on mean flow. The Reynolds stress acts as a bridge for transferring kinetic energy from mean flow at large scales to turbulence and cascading down to the smallest scale. In this picture, the random motion (turbulence) is continuously drawing energy from the coherent motion (mean flow) at large scale.

For SG-CFD, there does not exist a mean flow at the largest mass scale, where it is assumed to be isotropic and homogeneous. At the level of individual halos, the coherent motion (mean flow) of particles includes the halo radial and rotational motion. The kinetic energy associated with the coherent radial and rotational motion can be part of the virial kinetic energy  $\sigma_v^2$  and similarly cascaded across halos of different mass scales, which will be studied in this section. A complete analysis of the coherent motion in halos and energy transfer with random motion requires full knowledge of mean flow and dispersion of halos. This will be presented in a separate paper [M3].

Like the velocity vector, the particle position vector (Eq. (14)) can be decomposed as  $\mathbf{x}_p = \mathbf{x}_h + \mathbf{x}'_p$ , where  $\mathbf{x}_h$  is the (physical) position vector of the center of halo mass that particle reside in and  $\mathbf{x}'_p$  is the relative position of particles to center of mass. The halo radial and rotational motions can be defined by a halo (peculiar) virial quantity  $G_{hp}$  and angular momentum  $\mathbf{H}_h$  in physical coordinate (not comoving coordinate),

$$G_{hp} = \frac{1}{n_p} \sum_{i=1}^{n_p} (\mathbf{x}'_p \cdot \mathbf{u}'_p) \quad \text{and} \quad \mathbf{H}_h = \frac{1}{n_p} \sum_{i=1}^{n_p} (\mathbf{x}'_p \times \mathbf{u}'_p), \quad (56)$$

where  $\mathbf{u}'_p$  is the peculiar velocity. Both quantities are first order moment of velocity. Figure 12 presents the variation of the peculiar halo virial quantity  $G_{hp}$  and the angular momentum  $|\mathbf{H}_h|$  with halo group size  $n_p$ , where both increase with the halo size.

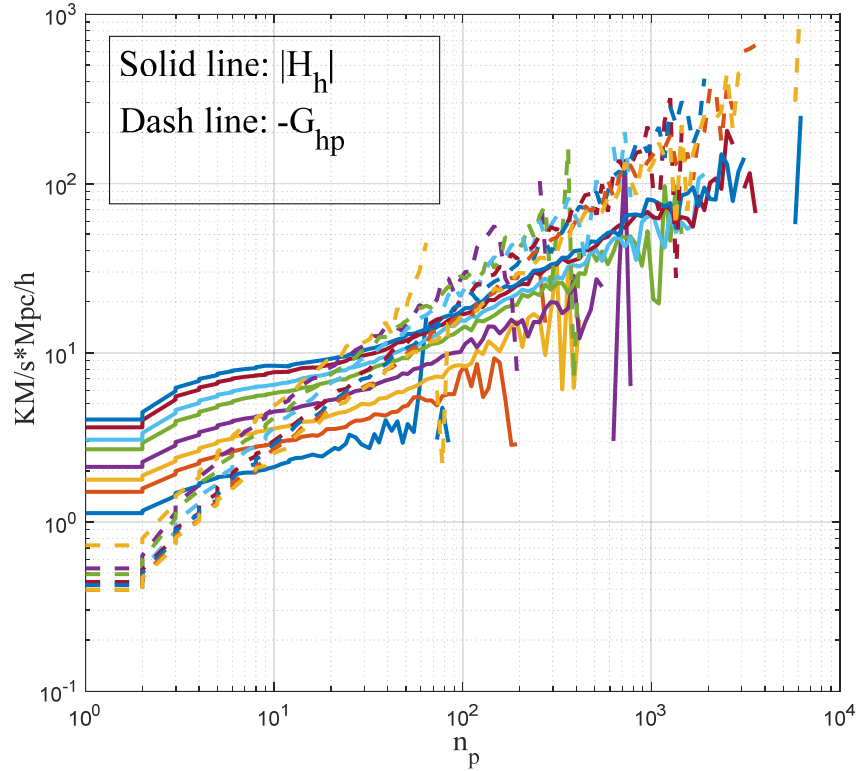


Figure 12. The variation of halo peculiar virial quantity  $G_{hp}(m_h, a)$  and angular momentum  $|\mathbf{H}_h(m_h, a)|$  with halo group size  $n_p$  for different redshifts  $z = 0, 0.1, 0.3, 0.5, 1.0, 1.5, 2.0,$  and  $3.0$ . For a give halo size, the virial quantity decreases with the scale factor  $a$  as  $G_{hp} \approx -f_G(m_h)a^{-1}Hr_g^2$ , while angular momentum increases with  $a$  as  $|\mathbf{H}_h| \approx f_H(m_h)a^{1/2}Hr_g^2$ .

$N$ -body simulations suggest the best expressions of,

$$G_{hp} \approx -f_G(m_h)a^{-0.85}Hr_g^2 \quad \text{and} \quad |\mathbf{H}_h| \approx f_H(m_h)a^{0.65}Hr_g^2, \quad (57)$$

where  $f_G(m_h) \in [1, 3]$  and  $f_H(m_h) \in [10, 1]$  are two functions of halo mass  $m_h$  only. It is expected that  $f_G(m_h)$  increases with  $m_h$  while  $f_H(m_h)$  decreases with  $m_h$  (Fig. 14). The limiting values of  $f_G(m_h)$  and  $f_H(m_h)$  can be derived for large and small halos [M3]. Another possible options for two quantities can be

$$G_{hp} \approx -f_G(m_h)a^{-1}Hr_g^2 \quad \text{and} \quad |\mathbf{H}_h| \approx f_H(m_h)a^{0.5}Hr_g^2, \quad (58)$$

where the mean square radius  $r_g$  for a given halo is defined as

$$r_g = \sqrt{\frac{\sum_{p=1}^{n_p} |\mathbf{x}'_p|^2}{n_p}}. \quad (59)$$

Here  $|\mathbf{x}'_p|$  is the distance of the  $p$ th particle to the center of mass. Compared to halo size  $r_h$  (virial radius that depends on the critical density ratio  $\Delta_c$ ), the mean square radius  $r_g$  is a well-defined quantity and easy to compute for every halo identified. For spherical halos of size  $r_h$  with a power-law density of  $\rho_h(r) \sim r^{-m}$ , the mean square radius can be found as

$$r_g = \sqrt{\frac{\int_0^{r_h} r^2 \rho_h(r) 4\pi r^2 dr}{\int_0^{r_h} \rho_h(r) 4\pi r^2 dr}} = \sqrt{\frac{3-m}{5-m}} r_h. \quad (60)$$

Figure 13 plots the variation of  $r_g$  with halo group size  $n_p$ , where the mean square radius scales as  $r_g \sim am_h^{1/3}$ . If the mean square radius can be related to the halo size as  $r_g = \gamma_g r_h$ , where  $\gamma_g$  is a dimensionless constant on the order of  $1/\sqrt{3}$  for a spherical halo (Eq. (60) with  $m=2$  for an isothermal density profile), we can conveniently write (average halo density is about  $\Delta_c$  times of the background density, i.e.  $\bar{\rho}_h = \Delta_c \bar{\rho}_0$ ) with a fitting formulae from simulation

$$r_g = \gamma_g a \left( \frac{2Gm_h}{\Delta_c H_0^2} \right)^{1/3} \quad \text{and} \quad \frac{r_g}{\text{Mpc}/h} \approx 0.28a \left( \frac{m_h}{2.27 \times 10^{13} M_\odot/h} \right)^{1/3}. \quad (61)$$

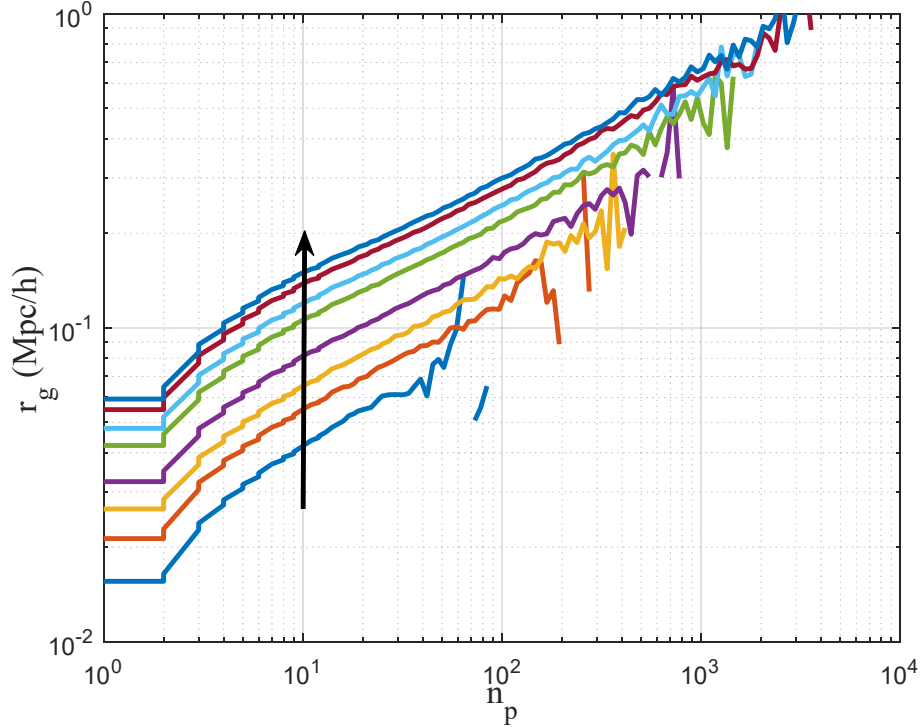


Figure 13. The variation of (physical) mean square radius  $r_g(m_h, a)$  with group size  $n_p$  for different redshifts  $z = 0, 0.1, 0.3, 0.5, 1.0, 1.5, 2.0,$  and  $3.0$  with arrow pointing to  $z=0$ . The mean square radius  $r_g \sim am_h^{1/3}$  is proportional to  $a$  and increasing with  $m_h$ .

The relation between  $G_{hp}$  and  $|\mathbf{H}_h|$  was predicted to scale as  $a^{-3/2}$  from a two-body collapse model (Eq. (104) in [19]). Here we can define a ratio  $\gamma_G$  between two quantities,

$$\gamma_G = \frac{-G_{hp}(m_h, a)a^{3/2}}{|\mathbf{H}_h(m_h, a)|} = \frac{f_G(m_h)}{f_H(m_h)}, \quad (62)$$

which quantifies the relative importance of radial motion to rotational motion. Figure 14 shows the variation of the ratio  $\gamma_G$  (red),  $f_G$  (black) and  $f_H$  (blue) in Eq. (57) with halo group size  $n_p$  for different redshifts  $z$ . All data from different redshifts collapse on to a single line for small halos. Note that  $\gamma_G \approx 1/(3\pi)$  for the smallest halos as predicted by the two-body collapse model (Eq. (104) in [19]). The ratio  $\gamma_G$  increases with halo size. Rotational motion is dominant over the radial motion for small halos and two motions are comparable for large halos. The large uncertainty for large halos might come from the lack of sufficient number of large halos.

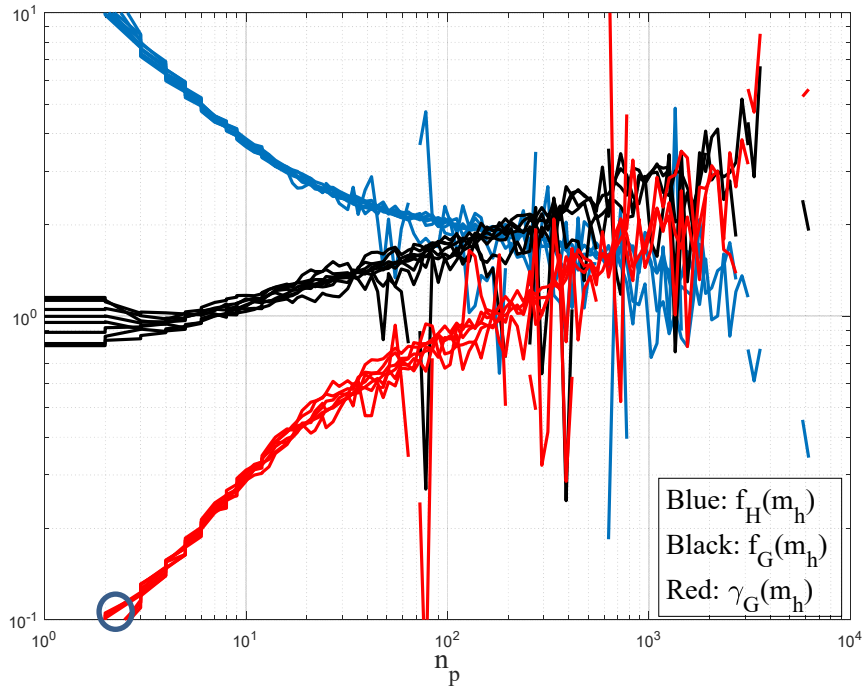


Figure 14. The variation of the ratio  $\gamma_G$  (red),  $f_G$  (black) and  $f_H$  (blue) with halo group size  $n_p$  for different redshifts  $z = 0, 0.1, 0.3, 0.5, 1.0, 1.5, 2.0,$  and  $3.0$ . All data from different redshifts collapse on a single line. For small halos,  $|\mathbf{H}_h(m_h, a)| \propto -G_{hp}(m_h, a)a^{3/2}$ . Note that  $\gamma_G \approx 1/(3\pi)$  (blue circle in figure) at the smallest scale as predicted by a two-



body collapse model (TBCM) [19]. The ratio  $\gamma_G$  and  $f_G$  increases with halo size, while  $f_H$  decreases with halo size.

The radius of gyration  $r_{rg}$  about any axis for a spherical halo with a power-law density is

$$r_{rg} = r_h \sqrt{\frac{2(3-m)}{3(5-m)}} = r_g \sqrt{\frac{2}{3}}. \quad (63)$$

An effective halo angular velocity  $\omega_h$  can be defined as (using Eq. (58)),

$$\omega_h = \frac{|\mathbf{H}_h|}{r_{rg}^2} = \frac{3|\mathbf{H}_h|}{2r_g^2} = \frac{3}{2} f_H(m_h) H_0 a^{-1}. \quad (64)$$

Figure 15 plots the variation of effective angular velocity  $\omega_h$  with halo size  $n_p$ . Small halos tend to have a greater angular velocity, while large halos approach a constant angular velocity between  $2 \sim 3H$ . Exact values will be presented for large halos (Table 3 in [M3]).

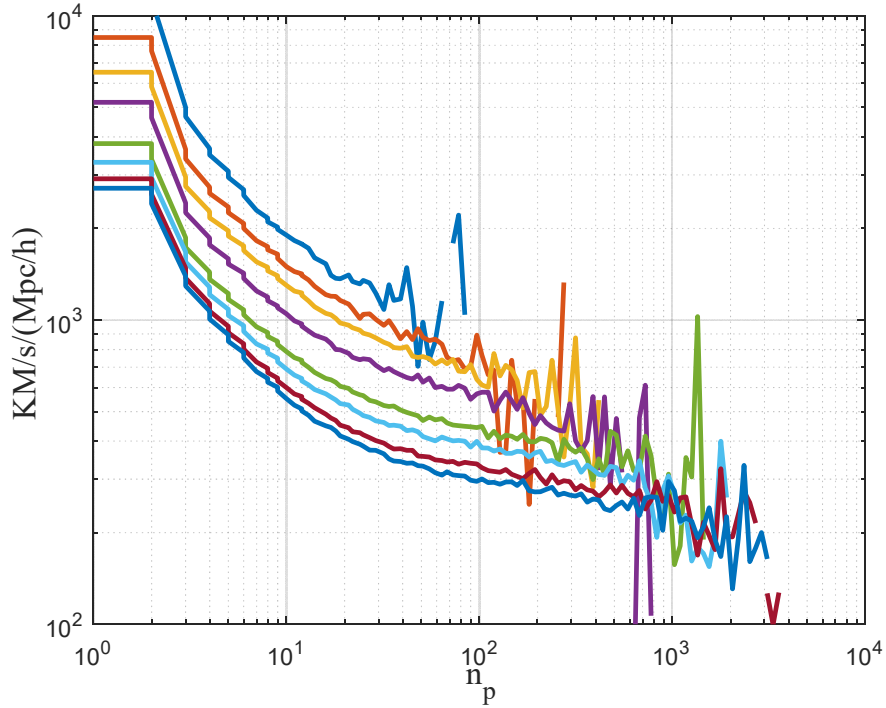


Figure 15. The variation of effective angular velocity  $\omega_h(m_h, a)$  with halo size for different redshifts  $z = 0, 0.1, 0.3, 0.5, 1.0, 1.5, 2.0,$  and  $3.0$ . Small halos tend to rotate much

faster, while the halo angular velocity approaches a constant value of  $2 \sim 3H$  for large halos.

The (peculiar) radial and rotational kinetic energies can be approximated as (Eqs. (58) and (61)),

$$K_{rp} = \frac{1}{2} \left( G_{hp} / r_g \right)^2 = \frac{1}{2} \gamma_g^2 a^{-3} \left[ f_G(m_h) \right]^2 \left[ \frac{2Gm_h H_0}{\Delta_c} \right]^{2/3}, \quad (65)$$

and

$$K_a = \frac{1}{2} |\mathbf{H}_h| \omega_h = \frac{3}{4} \left( |\mathbf{H}_h| / r_g \right)^2 = \frac{3}{4} \gamma_g^2 \left[ f_H(m_h) \right]^2 \left[ \frac{2Gm_h H_0}{\Delta_c} \right]^{2/3}. \quad (66)$$

Figure 16 presents the variation of the specific radial and rotational kinetic energies with halo size  $n_p$  for different redshifts  $z$ . For a given size of halo, the radial kinetic energy  $K_{rp}$  decreases with scale factor  $a$ , while the rotational kinetic energy  $K_a$  is relatively independent of time. Both radial and rotational kinetic energy increase with halo size.

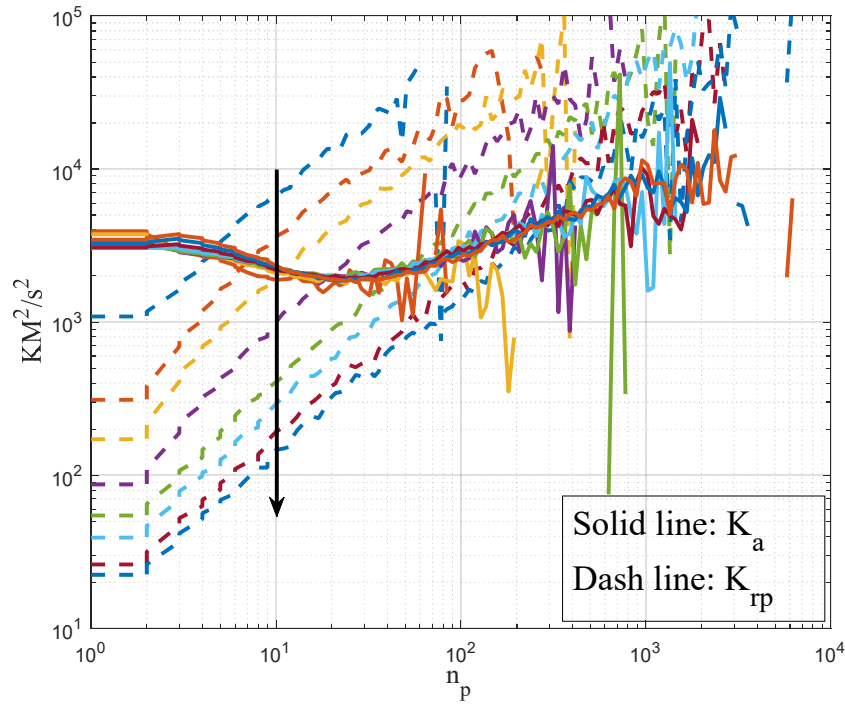


Figure 16. The variation of radial ( $K_{rp}$ ) and rotational kinetic energies ( $K_a$ ) with halo group size  $n_p$  for different redshifts  $z = 0, 0.1, 0.3, 0.5, 1.0, 1.5, 2.0,$  and  $3.0$ . For a given size of halo, radial peculiar kinetic energy  $K_{rp}$  is decreasing with scale factor  $a$ , while rotational kinetic energy  $K_a$  is relatively independent of time. Arrow points to  $z=0$ .

Figures 17 and 18 illustrate the variation of the flux functions for radial ( $\Pi_{urp}$ ) and rotational kinetic energies ( $\Pi_{ua}$ ) at different redshifts. Again, an inverse cascade is identified for both kinetic energies. The flux functions of radial and rotational motion are comparable to each other but is much smaller compared to the flux functions of halo virial and halo kinetic energies. From Eq. (44), the flux function of any quantity is proportional to that quantity  $V_s^L$  in typical halos. The rotational kinetic energy is estimated to be about 1% of the specific potential in the same halo (Table 3 [M3]). The flux function of rotational kinetic energy is also about 1% of the flux function of intra-halo potential, i.e.  $\Pi_{ua} \approx 0.01\Pi_{\phi_v}$  (see Fig. 8).

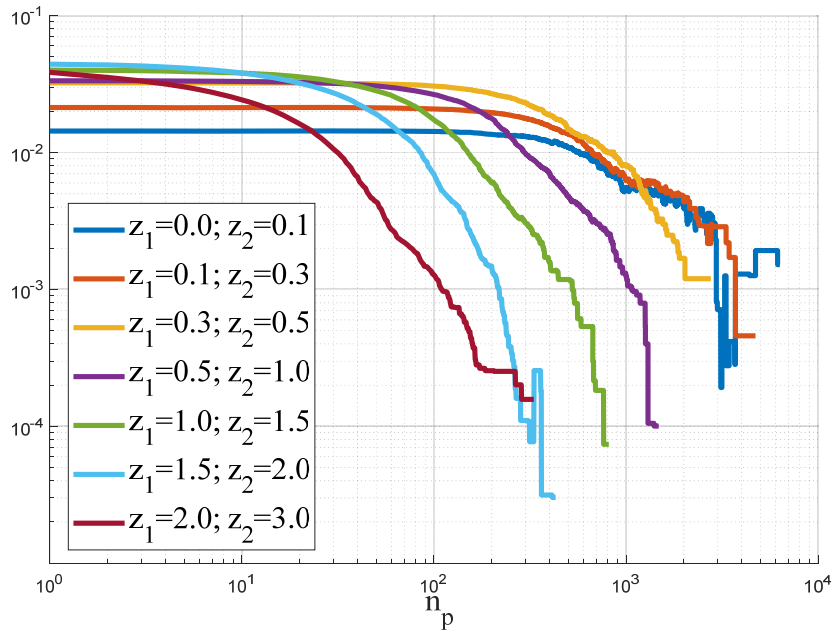


Figure 17. The variation of flux function  $\Pi_{ur}$  for halo radial kinetic energy  $K_{rp}(m_h, a)$  with halo group size  $n_p$ . The flux function  $\Pi_{ur} < 0$  (inverse cascade from small to large

scales) and is normalized by  $Nm_p u_0^2 / t_0$ . A scale-independent flux function can be identified for mass propagation range with  $m_h < m_h^*$ .

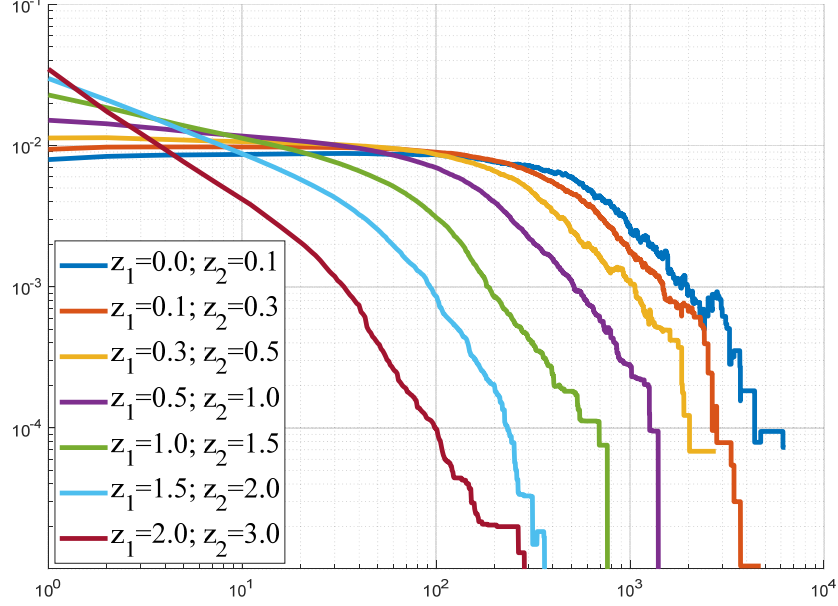


Figure 18. The variation of flux function  $\Pi_{ua}$  for halo rotational kinetic energy  $K_a(m_h, a)$  with halo group size  $n_p$ . The flux function  $\Pi_{ua} < 0$  (inverse cascade from large to small scales) and is normalized by  $Nm_p u_0^2 / t_0$ . A scale-independent flux function can be identified for mass propagation range with  $m_h < m_h^*$ .

## 5. The effect of halo shape on energy cascade

The shape of vortex plays a significant role for energy cascade in hydrodynamic turbulence. The shear-induced vortex stretching/elongating along the axis of rotation facilitates a direct energy cascade from large to small length scales. It should be of interest to check if the change of shape of halos, the counterpart of vortex in SG-CFD, plays a similar role for energy cascade in SG-CFD. Halos are usually assumed to be spherical. The standard method to model halos as ellipsoids is to construct a 3x3 inertia tensor  $I_{ij}$  for each halo [22],

$$I_{ij} = \sum_{p=1}^{n_p} x'_{p,i} x'_{p,j}, \quad (67)$$

where  $x'_{p,i}$  is the  $i$ th Cartesian component of the position vector  $\mathbf{x}'_p$  of a particle from the center of halo mass. Eigenvectors of the inertia tensor  $I_{ij}$  correspond to the directions of ellipsoid major axis, while the eigenvalues  $(r_{\lambda 1}, r_{\lambda 2}, r_{\lambda 3})$  correspond to the length of the semimajor axis. The inertial tensor can be constructed for every halo identified in the system, where the eigenvectors and eigenvalues can be determined for every halo identified.

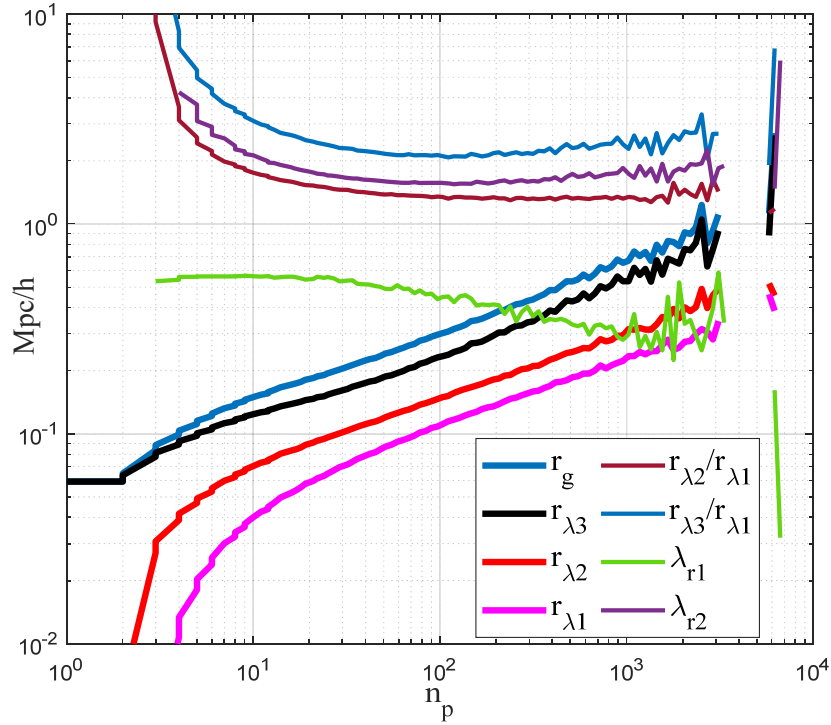


Figure 19. The variation of mean square radius  $r_g$  and three principle semiaxis of best fitting ellipsoid with  $r_{\lambda 3} > r_{\lambda 2} > r_{\lambda 1}$  at  $z=0$ . The ratio  $r_{\lambda 2}/r_{\lambda 1}$  rapidly decreases with halo size  $n_p$  to a constant value of 1.35 at around a characteristic mass scale  $n_p^* \approx 80$ , while the ratio  $r_{\lambda 3}/r_{\lambda 1}$  decreases to a minimum values of 2 and the slowly increase to 2.8 for halos  $n_p > n_p^*$ . The value of  $r_{\lambda 3}$  approaches  $r_g$  for small halos. The first ratio (Eq. (68))  $\lambda_{r1} \approx 0.5$  for small halos and  $\lambda_{r1} \approx 0.3$  for large halos. The second ratio  $\lambda_{r2}$  (Eq. (69)) is between [1.55

2], i.e the ellipsoid halos have a momentum of inertia about 1.55 to 2 times of that of a spherical halo with the same volume.

Figure 19 presents the variation of average length of three semimajor axis for the best fitting ellipsoid ( $r_{\lambda 3} > r_{\lambda 2} > r_{\lambda 1}$ ) with halo group size  $n_p$ . The average is taken over all halos from the same group. The mean square radius  $r_g$  is also presented in the same plot for comparison with the identity  $r_g^2 = r_{\lambda 1}^2 + r_{\lambda 2}^2 + r_{\lambda 3}^2$ . The ratio  $r_{\lambda 2}/r_{\lambda 1}$  rapidly decreases with halo size  $n_p$  to a constant value of  $\sim 1.35$  at around a characteristic mass scale  $n_p^* \approx 80$ , while the ratio  $r_{\lambda 3}/r_{\lambda 1}$  decreases to a minimum value of 2 and then slowly rise to about 2.8 for halos  $n_p > n_p^*$ . The other two critical ratios  $\lambda_{r1}$  and  $\lambda_{r2}$  can be introduced and plotted in the same figure. The first ratio is defined as,

$$\lambda_{r1} = \frac{r_{\lambda 2} - r_{\lambda 1}}{r_{\lambda 3} - r_{\lambda 2}}, \quad (68)$$

where  $\lambda_{r1} \approx 0.5$  is almost constant for small halos up to  $n_p = 40$  (Eq. (72) and green line in Fig. 21). This represents a unique evolution path of halo structure toward spherical shape. The second one is defined as the ratio of the moment of inertia of an ellipsoid rotating about the shortest semi-axis  $r_{\lambda 1}$  to that of a sphere with the same volume,

$$\lambda_{r2} = \frac{r_{\lambda 3}^2 + r_{\lambda 2}^2}{2(r_{\lambda 1} r_{\lambda 2} r_{\lambda 3})^{2/3}}, \quad (69)$$

where  $\lambda_{r2} = 1$  for spherical halos. Halo of an ellipsoid shape has a moment of inertia about  $\lambda_{r2} = 1.55$  to 2 times of that of a spherical halo with the same volume. Unlike the vortex stretching that can significantly change the momentum of inertia of vortex, the change of halo shape does not change the halo moment of inertia significantly and should not play a significant role in energy cascade. The long-range gravity and tidal effects in SG-CFD might not be strong enough to deform halos significantly. Note that vortex structure in incompressible flow is volume conserved with a

uniform density. Halos are growing in mass and volume with a nonuniform density profile in an environment lack of incompressibility. These unique features lead to different dominant mechanisms that halo and vortex should play in energy cascade. Halos cascade energy mostly through mass cascade or mass accretion (the growth of halo mass in Eq. (44)).

The shape of an ellipsoid can be systematically described by their triaxiality (prolate, oblate or triaxial), where a triaxiality parameter  $h_t$  is introduced [23]

$$h_t = \frac{r_{\lambda 3}^2 - r_{\lambda 2}^2}{r_{\lambda 3}^2 - r_{\lambda 1}^2}, \quad (70)$$

which quantifies whether a halo is prolate ( $h_t = 1$ ) or oblate ( $h_t = 0$ ). Other important halo shape parameters that can be derived from three principle eigenvalues are the ellipticity  $h_e$  and the prolateness  $h_p$  [24, 25]

$$h_e = \frac{r_{\lambda 3} - r_{\lambda 1}}{2(r_{\lambda 1} + r_{\lambda 2} + r_{\lambda 3})} \quad \text{and} \quad h_p = \frac{r_{\lambda 3} - 2r_{\lambda 2} + r_{\lambda 1}}{2(r_{\lambda 1} + r_{\lambda 2} + r_{\lambda 3})}, \quad (71)$$

where  $h_p = -h_e$  for oblate ellipsoid and  $h_p = h_e$  for prolate ellipsoid.

Figure 20 presents the variation of mean and standard deviation of halo shape parameters (the triaxiality  $h_t$ , ellipticity  $h_e$ , and prolateness  $h_p$ ) with halo group size  $n_p$  at  $z=0$ . Both shape parameters  $\langle h_e \rangle$  and  $\langle h_p \rangle$  have an initial sharp drop from 0.5 for  $n_p = 2$  to a minimum value, followed by a slow increase with halo size for large halos that do not have enough time to be completely virialized to a spherical shape. The mean triaxiality parameter  $\langle h_t \rangle$  decreases from 1 for  $n_p = 2$  to 0.75 and slowly rises to 0.8~0.9 for large halos. The value of  $h_t$  close to 1 indicates that a prolate shape should be dominant for large halos.

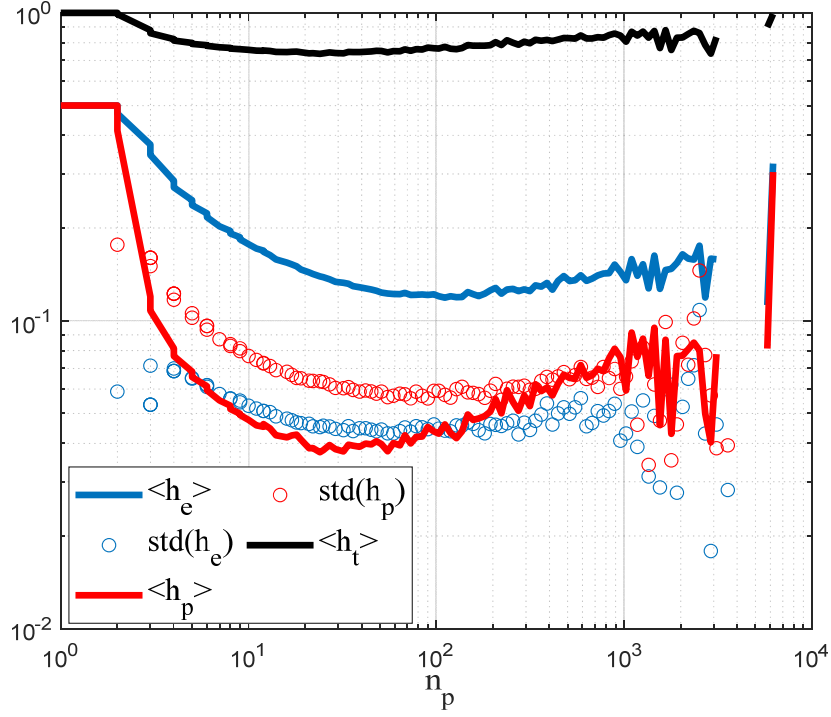


Figure 20. The variation of mean and standard deviation of halo shape parameters (the ellipticity  $h_e$  and the prolateness  $h_p$ ) with halo group size  $n_p$  at  $z=0$ . Both shape parameters  $\langle h_e \rangle$  and  $\langle h_p \rangle$  have an initial sharp decrease from 0.5 for  $n_p = 2$  to a minimum value at around the characteristic halo size  $n_p^* \approx 80$ , followed by a slow increase with halo size for halos greater than  $n_p^*$  that are not completely virialized. The triaxiality parameter  $\langle h_t \rangle$  decreases from 1 for  $n_p = 2$  to 0.75 and slowly rises to 0.8~0.9 for large halos.

To better describe the evolution of halo shape for growing halos, we present  $h_e$  and  $h_p$  on the same plot. Figure 21 plots the distribution of two halo shape parameter (the ellipticity  $h_e$  and the prolateness  $h_p$ ) for several different halo group sizes  $n_p = 2, 3, 10, 20$  at  $z=0$ . For the smallest halos  $n_p = 2$  with a line structure, all halos collapse onto the top right corner with  $h_e = h_p = 1/2$ . For halos  $n_p = 3$  with a planar structure, all halos collapse onto a straight line  $h_p = 3h_e - 1$  (blue line) with mean values of  $h_p = 1/8$  and  $h_e = 3/8$  for typical three-particle halos. The other two boundaries are also plotted as black lines for oblate ( $h_p = -h_e$ ) and prolate ( $h_p = h_e$ ) ellipsoids,



respectively. With increasing halo size  $n_p$ , the distribution of  $h_e$  and  $h_p$  for larger halos ( $n_p = 10$  and  $n_p = 20$  in figure) shrinks and quickly approaches the prolate boundary. Obviously, halos exhibit a range of shapes with a preference for prolateness over oblateness [26, 27]. This is expected as halos tend to form by collapsing along filaments and leading to prolateness.

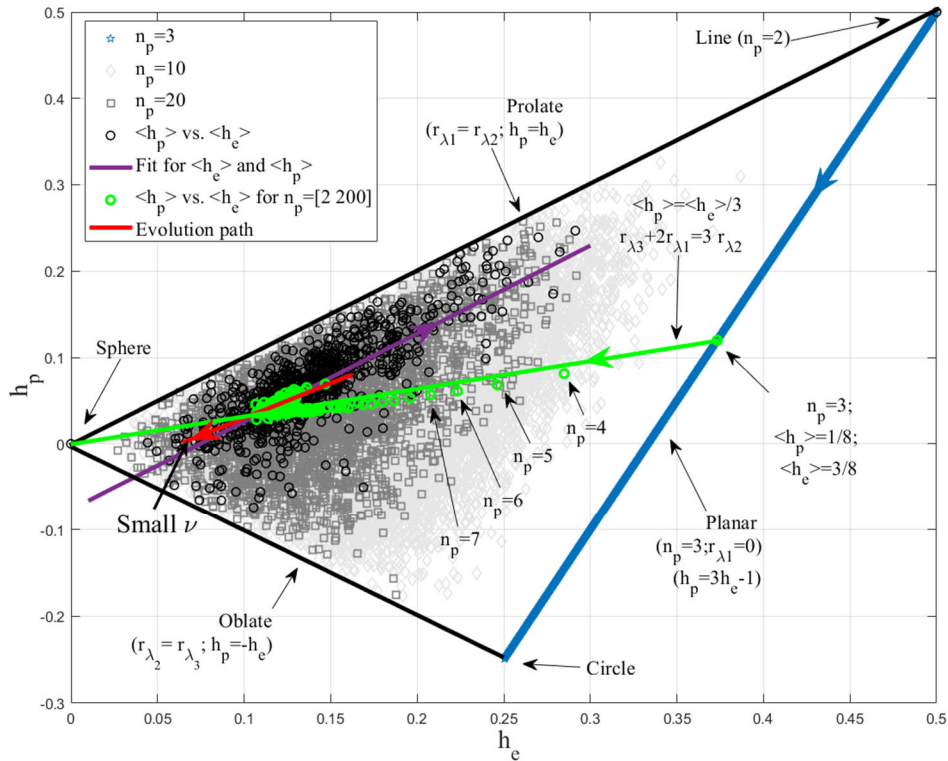


Figure 21. The distribution of two shape parameter (the ellipticity  $h_e$  and prolateness  $h_p$ ) for different group size  $n_p$  at  $z=0$ . All  $n_p = 2$  halos collapse on to the top right corner with  $h_e = h_p = 1/2$ . For all  $n_p = 3$  halos, the planar structure leads to a straight line  $h_p = 3h_e - 1$  (blue line) with mean values of  $h_p = 1/8$  and  $h_e = 3/8$ . The other two boundaries for  $h_e$  and  $h_p$  are also plotted as black lines for oblate and prolate ellipsoids, respectively. The mean shape parameters  $\langle h_e \rangle$  and  $\langle h_p \rangle$  for all halo groups of different sizes are presented as black circles (from Fig. 20), while green circles highlight the halos in range of  $n_p = [2, 200]$ . With increasing in size, the shape of halos evolves toward spherical structure along a unique path (green line:  $\langle h_p \rangle = \langle h_e \rangle / 3$ ) before a “V” turn. A fitted relation can be found  $\langle h_p \rangle = \langle h_e \rangle - 0.076$  (purple line) after “V” turn. The tip of “V” turn is identified as

$\langle h_e \rangle = 0.114$  and  $\langle h_p \rangle = 0.038$ . Red line with arrow pointing to low peak height  $\nu$  indicates the evolution path of halo shape from early stage to late stage.

The mean shape parameters  $\langle h_e \rangle$  and  $\langle h_p \rangle$  for all halo groups in Fig. 17 are presented as black circles. To better describe how the halo structure evolves with halo size, we plot  $\langle h_e \rangle$  and  $\langle h_p \rangle$  for halo sizes  $n_p$  between [2 200] (green circles). Clearly, the structure of halos evolves from  $n_p = 2$  to  $n_p = 3$  following the blue line (see arrows), and from  $n_p = 3$  to large halos around  $n_p^* = 80$  following the green line toward a spherical structure ( $h_p = h_e = 0$ ) with the equation,

$$\langle h_p \rangle = \langle h_e \rangle / 3 \quad \text{or} \quad r_{\lambda 3} + 2r_{\lambda 1} = 3r_{\lambda 2}, \quad (72)$$

which leads to  $\lambda_{r1} = 0.5$  (Eq. (68) and Fig. 19). This nearly perfect straight line of green circles is a clear indication that there exists a unique path for halo structure evolving from small size halos to characteristic size  $n_p^*$  or  $m_p^*$  that consistently approaches the spherical shape. For halos greater than the characteristic size  $n_p^*$  with faster mass accretion, there may not be enough time to relax to equilibrium. The halo structure evolution takes a “V” turn and follows the purple line. A fitted relation can be found as  $\langle h_p \rangle = \langle h_e \rangle - 0.076$  (parallel to the prolate boundary) with arrow pointing toward large halos.

The two shape parameters  $h_e$  and  $h_p$  can be conveniently expressed in terms of a reduced amplitude parameter (peak height)  $\nu = \delta_{cr} / \sigma(m_h, z)$  of density fluctuation [25],

$$h_e = 0.098 \log_{10} \nu + 0.094 \quad \text{and} \quad h_p = 0.079 \log_{10} \nu + 0.025, \quad (73)$$

where  $\delta_{cr} \approx 1.68$  is the critical overdensity from spherical collapse model and  $\sigma(m_h, z)$  is the rms fluctuation of the smoothed density field. To better describe the evolution path of a given halo

from early stage of its life with fast mass accretion (higher  $\nu$ ) to late stage with a stable core and slow mass accretion (lower  $\nu$ ), the evolution path for a range of  $\nu$  between [0.5 5] is also presented in the same plot (red line with arrow pointing to lower  $\nu$ ). Halos at their early stage with fast mass accretion are primarily of the prolate shape with increasing angular momentum with time. The mass accretion and increase of angular momentum will gradually slower down when halos evolve toward the late stage of their life along a path parallel to the prolate boundary and halos tend to be more spherical (red line in Fig. 21). However, the change of moment of inertia purely from the change of halo shape should not be significant. Most change of moment of inertia is from mass accretion during that evolution [M3]. By contrast, the shear-induced vortex stretching in hydrodynamic turbulence involves a path along the prolate boundary from “sphere” to “line” (Fig. 21), where moment of inertia changes significantly due to the shape change.

To explore the orientation of halo relative to the axis of rotation, Figure 22 illustrates the probability distribution of the angle  $\theta_{Hr}$  between axis of rotation (direction of angular momentum  $\mathbf{H}_h$ ) and the major principle axis ( $r_{\lambda 3}$ ) of triaxial ellipsoid halos for four halo groups of different sizes. The sharp peak around  $\theta_{Hr} = \pi/2$  indicates that most halos have their spin axis lying perpendicular to their major axis. A wider and broader distribution of angle  $\theta_{Hr}$  exists for larger halos. This finding agrees with previous results [26, 28, 29]. By contrast, the axis of rotation of vortex structure is usually aligned with the major axis of that vortex.

Halo interactions are local in mass space [1]. The halo structure evolution is predominantly a continuous process in halo mass space via sequential merging with single mergers. It is reasonable to expect larger halos to have a strong memory of their progenitors that they inherit their mass from (the green path in Fig. 21). For halos of  $n_p = 2$ , the axis of rotation must be perpendicular to the major axis and this feature is largely inherited with increasing halo sizes (see Fig. 22 for halos

with  $n_p = 3, 4, 5$  and 10). This also explains why halo tends to rotate around an axis perpendicular to its the major principal axis.

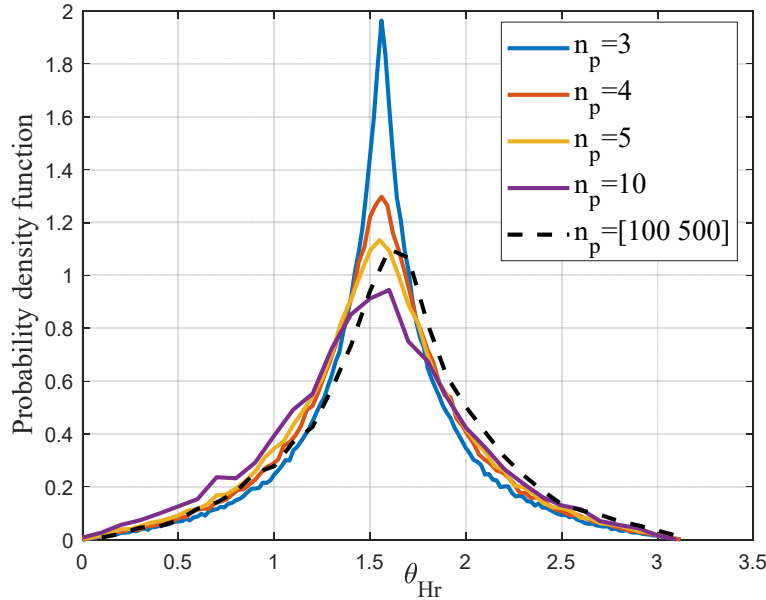


Figure 22. The probability density function of angle  $\theta_{Hr}$  between axis of rotation ( $\mathbf{H}_h$ ) and the major principal axis ( $\mathbf{r}_{\lambda_3}$ ) of triaxial ellipsoid halos. The axis of rotation of most halos is perpendicular to the major principal axis of ellipsoid.

In hydrodynamic turbulence, the vortex is stretching along the axis of rotation that facilitates the direct energy cascade, while the volume of vortex is conserved due to incompressibility, i.e. vortex more likely evolves along the prolate boundary toward a line structure in Fig. 21. For SG-CFD, halos smaller than the characteristic size  $m_h^*$  evolves along a unique path approaching the spherical shape (green line in Fig. 21). For halos greater than  $m_h^*$ , the halo shape evolves parallel to the prolate boundary. The tip of “V” turn with  $\langle h_e \rangle = 0.114$  and  $\langle h_p \rangle = 0.038$  in Fig. 21. The change of halo shape should not be the dominant mechanism for energy cascade. The situation is even more complicated for SG-CFD where the incompressibility condition does not apply. Due to the inverse mass cascade, both mass and volume of halos increases with time. Halo density is also

nonuniform. The shape change of halos does not play a dominant role on the energy cascade, while the halo mass accretion should be largely responsible for energy cascade (discussed in Section 4).

## 6. Conclusion

By revisiting fundamental ideas of the energy cascade of hydrodynamic turbulence, the energy cascade of self-gravitating collisionless fluid dynamics (SG-CFD) shares many similarities, but also exhibits many unique features. This paper formulates the energy cascade for self-gravitating collisionless fluid system (SG-CFD). The starting point is a halo-based self-gravitating collisionless system that can be divided into a halo and out-of-halo sub-systems. The particle motion can be decomposed into the motion of halo and the motion in halo. Virial equilibrium is established for both motions, while equilibrium for particle motion in halo is established earlier than the random motion of halo (Fig. 9). Total energy of out-of-halo sub-system is conserved with time, where potential cancels the kinetic energy with an effective virial ratio of 2 (Figs. 6 and 9). The energy change in the entire system mostly comes from the virilization in halo sub-system. The total kinetic/potential energies in halo-sub system increase  $\sim t$  with scale- and time-independent flux functions in mass propagation range once the statistically steady state is established. (Figs. 10 and 11). A continuous mass exchange between two sub-systems at the smallest scale is required to sustain the growth of total halo mass as  $M_h \sim a^{1/2}$  and the linear growth of total halo energy  $E \sim a^{3/2}$  (Figs. 9-11).

The mass exchange between two sub-systems drives the mass cascade in halo sub-system. By introducing the energy flux and transfer functions, an inverse cascade of kinetic energy in halo sub-system is identified with kinetic energy injected at the smallest scale and transferred from small to large mass scales, and vice versa for potential energy with a direct cascade (Figs. 3, 4, 7, and 8). Both cascades are related by the virial theorem. The direct cascade of potential energy

sustains the inverse cascade of kinetic energy. Both potential and kinetic energies exhibit a scale- and time-independent flux in the mass propagation range with energy flux proportional to the mass flux (Eqs. (27) and (48)). The coherent motion within halos includes the halo radial and rotational motion. By correctly modeling the dependence of halo radial and rotational moment and angular velocity on halo mass (Eqs. (58), (64), and (65) and (66) and Figs. 12, 14, 15 and 16), an inverse cascade can also be identified for the kinetic energy from coherent radial and rotational motion (mean flow) in halos (Figs. 17 and 18). For a given mass of halos, the rotational kinetic energy is independent of time, while the radial (peculiar) kinetic energy decreases with time (Eqs. (65) and (66)). The flux function of a general specific quantity is also formulated (Eqs. (39) and (40)). In SG-CFD, the energy cascade is mostly facilitated by the mass accretion of typical halos from small to large mass scales (Eq. (44)). By contrast, the vortex stretching/elongating along its axis of rotation facilitates a direct energy cascade from large to small length scales in hydrodynamic turbulence. The vortex is volume conserved with a uniform density due to the incompressibility. The axis of rotation is usually aligned with the major axis of vortex.

The shape evolution of halos is also extensively studied for SG-CFD. The halo structure evolution is continuous in mass space with halos inheriting structures from their progenitors. The shape of halos evolves along a unique path gradually approaching the spherical shape with increasing halo size (green line in Fig. 21). Large halos exhibit a range of shapes with a preference for prolateness over oblateness and most halos have their spin axis lying perpendicular to their major axis (Fig. 22). Halos become more spherical at the late stage with slower mass accretion (red line in Fig. 21 and Eq. (73)). However, the effect of halo shape change does not play a significant role on energy cascade with the variation of moment of inertial less than 2 times from shape change (Eq. (69) and Fig. 19). Finally, this paper focus on the energy transfer and cascade

across halos of different mass scales, while future study should extend to the energy transfer within individual halos that requires complete solutions of the mean flow and velocity dispersions.

## Reference

1. Xu, Z., *Inverse mass cascade of self-gravitating collisionless flow and effects on halo mass functions*. arXiv:2109.09985v1 [astro-ph.CO], 2021.
2. Xu, Z., *Inverse mass cascade of self-gravitating collisionless flow and effects on halo deformation, energy, size, and density profiles*. arXiv:2109.12244v1 [astro-ph.CO], 2021.
3. Richardson, L.F., *Weather Prediction by Numerical Process*. 1922, Cambridge, UK: Cambridge University Press.
4. Kolmogoroff, A., *The local structure of turbulence in incompressible viscous fluid for very large Reynolds numbers*. Comptes Rendus De L Academie Des Sciences De L Urss, 1941. **30**: p. 301-305.
5. Kolmogoroff, A.N., *Dissipation of energy in the locally isotropic turbulence*. Comptes Rendus De L Academie Des Sciences De L Urss, 1941. **32**: p. 16-18.
6. Taylor, G.I., *The transport of vorticity and heat through fluids in turbulent motion*. Proceedings of the Royal Society of London Series a-Containing Papers of a Mathematical and Physical Character, 1932. **135**(828): p. 685-705.
7. Taylor, G.I., *Production and dissipation of vorticity in a turbulent fluid*. Proceedings of the Royal Society of London Series a-Mathematical and Physical Sciences, 1938. **164**(A916): p. 0015-0023.
8. Andersson, B. and R. Andersson *Computational Fluid Dynamics for Engineers*. 2012, New York: Cambridge University Press.
9. Kraichnan, R.H., *Inertial Ranges in 2-Dimensional Turbulence*. Physics of Fluids, 1967. **10**(7): p. 1417-+.
10. Padmanabhan, T., *Statistical-Mechanics of Gravitating Systems*. Physics Reports-Review Section of Physics Letters, 1990. **188**(5): p. 285-362.
11. Xu, Z., *The maximum entropy distributions of collisionless particle velocity, speed, and energy for statistical mechanics of self-gravitating collisionless flow (SG-CFD)*. arXiv:2110.03126v1 [astro-ph.CO], 2021.
12. Xu, Z., *Mass functions of dark matter halos from maximum entropy distributions for self-gravitating collisionless flow*. arXiv:2110.09676v1 [astro-ph.CO], 2021.
13. Neyman, J. and E.L. Scott, *A Theory of the Spatial Distribution of Galaxies*. Astrophysical Journal, 1952. **116**(1): p. 144-163.
14. Cooray, A. and R. Sheth, *Halo models of large scale structure*. Physics Reports-Review Section of Physics Letters, 2002. **372**(1): p. 1-129.
15. C. S. Frenk, et al., *Public Release of N-body simulation and related data by the Virgo consortium*. arXiv:astro-ph/0007362v1 2000.
16. Jenkins, A., et al., *Evolution of structure in cold dark matter universes*. Astrophysical Journal, 1998. **499**(1): p. 20.
17. Colberg, J.M., et al., *Linking cluster formation to large-scale structure*. Monthly Notices of the Royal Astronomical Society, 1999. **308**(3): p. 593-598.
18. Sheth, R.K., H.J. Mo, and G. Tormen, *Ellipsoidal collapse and an improved model for the number and spatial distribution of dark matter haloes*. Monthly Notices of the Royal Astronomical Society, 2001. **323**(1): p. 1-12.
19. Xu, Z., *A non-radial two-body collapse model (TBCM) for gravitational collapse of dark matter in expanding background and generalized stable clustering hypothesis (GSCP)*. arXiv:2110.05784v1 [astro-ph.CO], 2021.
20. Gunn, J.E., *Massive Galactic Halos .1. Formation and Evolution*. Astrophysical Journal, 1977. **218**(3): p. 592-598.



21. Bryan, G.L. and M.L. Norman, *Statistical properties of X-ray clusters: Analytic and numerical comparisons*. *Astrophysical Journal*, 1998. **495**(1): p. 80-99.
22. Springel, V., S.D.M. White, and L. Hernquist, *The shapes of simulated dark matter halos*. *Dark Matter in Galaxies*, 2004(220): p. 421-429.
23. Franx, M., G. Illingworth, and T. Dezeew, *The Ordered Nature of Elliptic Galaxies - Implications for Their Intrinsic Angular Momenta and Shapes*. *Astrophysical Journal*, 1991. **383**(1): p. 112-134.
24. Bardeen, J.M., et al., *The Statistics of Peaks of Gaussian Random-Fields*. *Astrophysical Journal*, 1986. **304**(1): p. 15-61.
25. Despali, G., C. Giocoli, and G. Tormen, *Some like it triaxial: the universality of dark matter halo shapes and their evolution along the cosmic time*. *Monthly Notices of the Royal Astronomical Society*, 2014. **443**(4): p. 3208-3217.
26. Allgood, B., et al., *The shape of dark matter haloes: dependence on mass, redshift, radius and formation*. *Monthly Notices of the Royal Astronomical Society*, 2006. **367**(4): p. 1781-1796.
27. Tormen, G., *The rise and fall of satellites in galaxy clusters*. *Monthly Notices of the Royal Astronomical Society*, 1997. **290**(3): p. 411-421.
28. Shaw, L.D., et al., *Statistics of physical properties of dark matter clusters*. *Astrophysical Journal*, 2006. **646**(2): p. 815-833.
29. Bailin, J. and M. Steinmetz, *Internal and external alignment of the shapes and angular momenta of  $\Lambda$ CDM halos*. *Astrophysical Journal*, 2005. **627**(2): p. 647-665.

Inverse and direct cascade of kinetic and potential energy for self-gravitating collisionless dark matter flow and effects of halo shape on energy cascade

Zhijie (Jay) Xu<sup>1,a</sup>

1. Computational Mathematics Group, Physical and Computational Sciences Directorate, Pacific Northwest National Laboratory, Richland, WA 99352, USA

---

<sup>a</sup>) Electronic mail: [zhijie.xu@pnl.gov](mailto:zhijie.xu@pnl.gov); [zhijiexu@hotmail.com](mailto:zhijiexu@hotmail.com)

|   |   |
|---|---|
| Contents                                |   |
| Nomenclature .....                      | 3 |
| The simulation and numerical data ..... | 7 |

## Nomenclature

| Symbol        | S.I. Unit            | Physical Meaning  |
|---------------|----------------------|---|
| $\Omega_0$    | Dimensionless        | Matter content  |
| $\Lambda$     | $1/m^2$              | Universe constant   |
| $h$           | Dimensionless        | Dimensionless Hubble constant   |
| $\Gamma$      | Dimensionless        | $\Gamma = \Omega_0 h$ Shape parameter for the density power spectrum  |
| $\sigma_8$    | Dimensionless        | Density fluctuation at $r = 8Mpc/h$   |
| $L$           | $m$                  | Size of the simulation box  |
| $N$           | Dimensionless        | Total number of particles in the simulation   |
| $M$           | $kg$                 | Total mass of the entire system   |
| $m_p$         | $kg$                 | Mass of a collisionless particle  |
| $l_{soft}$    | $m$                  | Gravitational softening length  |
| $V$           | $m^3$                | Volume of the simulation box  |
| $u(t), u_0$   | $m/s$                | One-dimensional velocity dispersion of the entire system at time $t$ and $z=0$                              |
|               |                      |   |
| $n$           | Dimensionless        | Exponent of the interaction potential. Specifically, $n=-1$ represents the usual gravitational interaction. |
| $n_{ps}$      | Dimensionless        | Effective index of power spectrums of density fluctuations  |
| $G$           | $m^3/(kg \cdot s^2)$ | Gravitational constant  |
| $a, z$        | Dimensionless        | Scale factor and redshift $a = 1/(1+z)$   |
| $H_0, H$      | $1/s$                | Hubble constants ('0' stands for the current epoch)   |
| $t_0, t$      | $s$                  | Physical time ('0' stands for the current epoch)  |
| $N_h$         | Dimensionless        | Total number of halos in the system   |
| $M_o(a)$      | $kg$                 | Total mass of out-of-halo sub-system  |
| $M_h(a)$      | $kg$                 | Total mass of halo sub-system   |
| $m_g(m_h, a)$ | $kg$                 | Total mass of a halo group of the same size halos of mass $m_h$   |
| $m_h$         | $kg$                 | Mass of a specific halo   |
| $n_h$         | Dimensionless        | Number of halos in a halo group   |
| $n_p$         | Dimensionless        | Number of particles in a halo   |
| $m_h^*$       | $kg$                 | Characteristic mass scale   |
| $m_h^L$       | $kg$                 | Mass of a typical halo  |
| $r_h$         | $m$                  | The virial radius (size) of spherical halos   |
|               |                      |   |

|                                      |                    |   |
|--------------------------------------|--------------------|---|
| $\Pi_m(m_h, a)$                      | $kg/s$             | Mass flux function  |
| $\varepsilon_m(a)$                   | $kg/s$             | Mass flux function for mass propagation range                           |
| $f_M(m_h, m_h^*)$                    | $1/kg$             | Halo mass function  |
| $T_m(m_h, a)$                        | $1/s$              | Real-space mass transfer function                                       |
| $f_h(m_h, a)$                        | $1/s$              | Frequency of halo merging for a halo group of size $m_h$                |
| $f_0(a)$                             | $1/s$              | Fundamental frequency of halo merging                                   |
| $\tau_g(m_h, a)$                     | $s$                | Mean time to cascade mass of a halo group of size $m_h$                 |
| $\tau_h(m_h, a)$                     | $s$                | Mean waiting time (lifespan) for a halo in halo group of size $m_h$     |
| $n_p^*, n_p^L$                       | Dimensionless      | Number particles in a halo of mass $m_h^*$ and $m_h^L$                  |
| $n_h^*, n_h^L$                       | Dimensionless      | Number of halos in a halo group of size $m_h^*$ and $m_h^L$             |
| $\alpha_0$                           | Dimensionless      | Numerical constant for the mass flux function (order of unity)          |
| $\tau_0$                             | Dimensionless      | Scaling exponent for the fundamental frequency $f_0(a)$                 |
| $\lambda$                            | Dimensionless      | Halo geometry parameter   |
| $\lambda_m$                          | Dimensionless      | Scaling exponent for the mass of typical halo $m_h^L$                   |
|                                      |                    |   |
| $\mathbf{u}_p$                       | $m/s$              | Peculiar velocity vector of a collisionless particle                    |
| $\mathbf{u}_h$                       | $m/s$              | Peculiar velocity of a halo   |
| $\mathbf{u}_p'$                      | $m/s$              | Fluctuation of particle (peculiar) velocity                             |
| $\mathbf{x}_p$                       | $m$                | The position vector of a collisionless particle                         |
| $\mathbf{x}_h$                       | $m$                | The position vector of the center of mass of a given halo               |
| $\mathbf{x}_p'$                      | $m$                | The relative position vector to the halo center of mass                 |
| $\sigma_v^2(m_h)$                    | $m^2/s^2$          | The halo virial velocity dispersion for halo group of mass $m_h$        |
| $\sigma_h^2(m_h)$                    | $m^2/s^2$          | The halo velocity dispersion for halo group of mass $m_h$               |
| $\beta_{\sigma_h}, \beta_{\sigma_v}$ | Dimensionless      | The coefficients for fitting relations of $\sigma_v^2$ and $\sigma_h^2$ |
|                                      |                    |   |
| $\Pi_{kh}(m_h, a)$                   | $kg \cdot m^2/s^3$ | The real-space halo kinetic energy flux function                        |
| $\varepsilon_{kh}(a)$                | $kg \cdot m^2/s^3$ | The scale-independent halo kinetic energy flux                          |
| $\sigma_{hg}^2(m_h, a)$              | $m^2/s^2$          | The total halo kinetic energy of a halo group of mass $m_h$             |
|                                      |                    |   |
| $V_s(m_h, a)$                        |                    | A generic specific variable for general formulation of cascade          |
| $\Pi_{vs}(m_h, a)$                   |                    | The flux function of $V_s$  |
| $\varepsilon_{vs}(a)$                |                    | The scale-independent flux function of $V_s$                            |
| $T_{vs}(m_h, a)$                     |                    | The transfer function of $V_s$  |

|                        |                    |   |
|------------------------|--------------------|---|
| $\lambda_m$            | Dimensionless      | The exponent for mass of a typical halo, i.e. $m_h^L \sim a^{\lambda_m}$                    |
| $\lambda_v$            | Dimensionless      | The exponent for the mean of quantity $V_s$ , i.e. $\langle V_s \rangle \sim a^{\lambda_v}$ |
|                        |                    |   |
| $\Pi_{kv}(m_h, a)$     | $kg \cdot m^2/s^3$ | The real-space virial kinetic energy flux function  |
| $\varepsilon_{kv}(a)$  |                    | The scale-independent halo virial energy flux   |
| $T_{kh}(m_h, a)$       | $m^2/s^3$          | The real-space transfer function of halo kinetic energy                                     |
| $\phi_i$               | $m^2/s^2$          | The specific potential for particle $i$   |
| $\phi_{ih}, \phi_{iv}$ | $m^2/s^2$          | The specific inter- and intra-halo potential for particle $i$                               |
| $\phi_{hh}, \phi_{hv}$ | $m^2/s^2$          | The specific inter- and intra-halo potential for a given halo                               |
| $\phi_h(m_h, a)$       | $m^2/s^2$          | The specific inter-halo gravitational potential for a halo group                            |
| $\phi_v(m_h, a)$       | $m^2/s^2$          | The specific intra-halo gravitational potential for a halo group                            |
| $\Pi_{\phi_h}$         | $kg \cdot m^2/s^3$ | The real-space inter-halo potential energy flux function                                    |
| $\Pi_{\phi_v}$         | $kg \cdot m^2/s^3$ | The real-space intra-halo potential energy flux function                                    |
| $\gamma_v$             | Dimensionless      | The virial ratio for motion of particles within individual halos                            |
| $\gamma_h$             | Dimensionless      | The virial ratio for motion individual halos  |
| $\gamma_{ho}$          | Dimensionless      | The virial ratio for motion of particles in out-of-halo sub-system                          |
| $\sigma_{ho}^2$        | $m^2/s^2$          | The velocity dispersion of particles in out-of-halo sub-system                              |
| $\phi_{ho}$            | $m^2/s^2$          | The specific potential of particles in out-of-halo sub-system                               |
| $L_h$                  | $m/s$              | The specific radial linear momentum of halos  |
| $L_{hp}$               | $m/s$              | The specific (peculiar) radial linear momentum of halos                                     |
| $G_h$                  | $m^2/s$            | The specific virial quantity of halos   |
| $G_{hp}$               | $m^2/s$            | The specific (peculiar) virial quantity of halos  |
| $\mathbf{H}_h$         | $m^2/s$            | The specific angular momentum vector of halos   |
| $f_G(m_h)$             | Dimensionless      | Coefficient of $G_{hp}$ as a function of halo mass $m_h$                                    |
| $f_H(m_h)$             | Dimensionless      | Coefficient of $ \mathbf{H}_h $ as a function of halo mass $m_h$                            |
| $r_g(m_h, a)$          | $m$                | The mean square radius of a given halo  |
| $\gamma_g$             | Dimensionless      | The ratio between mean square radius and halo size $r_g/r_h$                                |
| $r_{rg}(m_h, a)$       | $m$                | The radius of gyration about any axis for a spherical halo                                  |
| $\gamma_G$             | Dimensionless      | Ratio quantifies the importance of radial and rotational motion                             |
| $\omega_h$             | $1/s$              | The halo angular velocity   |
| $\Pi_{wrp}$            | $kg \cdot m^2/s^3$ | The real-space radial (peculiar) kinetic energy flux function                               |
| $\Pi_{ua}$             | $kg \cdot m^2/s^3$ | The real-space rotational energy flux function  |
|                        |                    |   |

|   |               |   |
|---|---------------|---|
| $I_{ij}$                                      | $m^2$         | The halo inertial tensor for shape analysis   |
| $r_{\lambda 1}, r_{\lambda 2}, r_{\lambda 3}$ | $m$           | Three eigenvalues of tensor $I_{ij}$ , i.e. the length of semimajor axis of the best ellipsoid fitting the shape of halos |
| $h_t$   | Dimensionless | The triaxiality parameter, $h_t = 1$ for prolate and $h_t = 0$ for oblate   |
| $h_e$   | Dimensionless | The ellipticity parameter   |
| $h_p$   | Dimensionless | The prolateness parameter, $h_p = h_e$ for prolate ellipsoid and $h_p = -h_e$ for oblate ellipsoid                        |
| $\nu$   | Dimensionless | Halo peak height parameter  |
| $\lambda_r$                                   | Dimensionless | Ratio between the length of three semimajor axis  |
|   |               |   |

## The simulation and numerical data

The numerical data for this work is publicly available and generated from the  $N$ -body simulations carried out by the Virgo consortium, an international collaboration that aims to perform large  $N$ -body simulations of the formation of large-scale structures. A comprehensive description of the simulation data can be found in [1, 2]. As a first step, the current work focuses on the matter-dominant gravitational collapse of collisionless particles using simulations where  $\Omega_0 = 1$  and a standard CDM power spectrum (SCDM). A similar analysis can be extended to other simulations with different model assumptions and parameters in the future.

The same set of simulation data has been widely used in a number of different studies from clustering statistics [2] to the formation of halo clusters in large scale environments [3], and testing models for halo abundance and mass functions [4]. The simulation includes over  $N = 256^3$  particles with mass  $m_p = 2.27 \times 10^{11} M_\odot / h$ . The simulation box size is around 240 Mpc/h, where  $h$  is the dimensionless Hubble constant in the unit of  $100 \text{ km}/\text{Mpc} \cdot \text{s}$ .

Some key parameters of the  $N$ -body simulations are listed in Table 1. The friends-of-friends algorithm (FOF) was used to identify all halos from the simulation data that depends only on a dimensionless parameter  $b$ , which defines the linking length  $b(N/V)^{-1/3}$ , where  $V$  is the volume of the simulation box. Halos were identified with a linking length parameter of  $b = 0.2$  in this work. All halos identified from the simulation data are first grouped into halo groups of different sizes according to the mass of halos  $m_h$  (or in terms of  $n_p$ , the number of particles in the halo), where  $m_h = n_p m_p$ . The total mass for a halo group of mass  $m_h$  is introduced as  $m_g = m_h n_h$ , where  $n_h$  is the number of halos in that group. Simulation results will be presented to describe the energy cascade across halo groups at different mass scales.



Table S1. Numerical parameters of  $N$ -body simulation for SCDM

| $\Omega_0$ | $\Lambda$ | $h$ | $\Gamma$ | $\sigma_8$ | $L(Mpc/h)$ | $N$     | $m_p(M_\odot/h)$      | $l_{soft}(Kpc/h)$ | $u_0(Km/s)$ |
|------------|-----------|-----|----------|------------|------------|---------|-----------------------|-------------------|-------------|
| 1.0        | 0.0       | 0.5 | 0.5      | 0.51       | 239.5      | $256^3$ | $2.27 \times 10^{11}$ | 36                | 354.6       |

## Reference

1. C. S. Frenk, et al., *Public Release of N-body simulation and related data by the Virgo consortium*. arXiv:astro-ph/0007362v1 2000.
2. Jenkins, A., et al., *Evolution of structure in cold dark matter universes*. *Astrophysical Journal*, 1998. **499**(1): p. 20.
3. Colberg, J.M., et al., *Linking cluster formation to large-scale structure*. *Monthly Notices of the Royal Astronomical Society*, 1999. **308**(3): p. 593-598.
4. Sheth, R.K., H.J. Mo, and G. Tormen, *Ellipsoidal collapse and an improved model for the number and spatial distribution of dark matter haloes*. *Monthly Notices of the Royal Astronomical Society*, 2001. **323**(1): p. 1-12.